Conference Proceedings

The Kabarak University International Conference on the Basic Sciences

KLAW Conference Center, Kabarak University, Kenya

Sponsored by

Contents

High-Performance Computing in Materials Science

George Amolo (Phd, Wits)
Department of Physics and Space Sciences
The Technical University of Kenya, PO Box 52428 00200, Nairobi
georgeamolo862@gmail.com / george.amolo@tukenya.ac.ke

Abstract

Computational modeling in materials science involves the employment of fundamental physical and life sciences as well as computer science to study the properties of matter at the microscopic level. Such studies can be carried out by electronic or atomistic approaches and the outcomes used to complement the applied sciences as well as to guide experimental research work. Over the last decade, affordable computing resources coupled with community developed state-of-the-art codes are available for graduate students and research staff even in the developing world, where there is limited funding. This has been made possible through collaborative research or via initiatives from friendly partners in Europe and America. It is, therefore, possible to engage in quality research for capacity building or the development of products and services. Computational modeling can now predict, independently, outcomes of some materials properties to within accuracies of less than 5% compared with independent experimental techniques. This implies that computational modeling can be used as a decision support tool, enabling tests before production, hence cutting down costs from the previous trial and error approaches. Current problems in science and technology require a multidisciplinary approach such as that being employed in computational modeling and hence its applications in both fundamental and applied sciences. Due to the accessibility of resources to perform research using computational modeling in materials and other applied sciences, additional effort needs to be made to involve more graduate students and faculty in these areas for capacity building. In due course, it is expected that the research capacity realized will be focused to solve current and emerging problems in this country.

1.0 Introduction

Computational modeling in materials science is the use of computer science, fundamental biology, chemistry, mathematics, and physics to study the properties matter. Research studies in materials science that can benefit from computational modeling include both fundamental and the applied sciences. High-Performance Computing (HPC) is the application of dedicated and coordinated computer resources over a period of time to solve research problems that require massive computer speeds and memory. Computational modeling has evolved from traditional and basic problems to a state-of-the-art technique used as a decision support tool in materials science research. The results of carefully thought out and executed research problems are informative as well as accepted by the scientific community through dissemination in presentations and peer-reviewed journal publications.

Graduate students and academic staff in countries where there is limited or no funding for experimental approaches to carry out research as well as research groups that have standard and well maintained experimental infrastructure who need results of simulations of their systems to seek insights into their work are likely to greatly benefit from this approach. A beginner requires a standard desktop computer with 2 – 8 Mb Ram, at least 500 Gb of hard disk space or a laptop of similar specifications with basic computer knowledge. Having a laptop has the advantage of easy movement to interact with others. While having a windows operating system to take advantage of

free software is sufficient, graduate students and younger faculty are strongly encouraged to have open-source operating software installed in the desktop or laptop. It should be noted that most software running on the open-source system are free and do not require a license. A learner should be prepared to invest at least three months to be comfortable with navigation on the open-source system and to learn to use basic system commands in order to run beginner calculations on properties of well-known materials. Competence beyond that, even at the first-degree level, requires more investment in time but leads to comfort in the understanding of scientific concepts and interpretation of results.

2.0 Resources needed for research engagement in computational modeling in materials science

To undertake research on larger problems that require additional computational resources above a desktop/laptop one has to look to other providers. At the national level, The Kenya Education Network (KENET) provides graduate students and faculty-specific cloud services and training with arrangement for calculations [1]. The African School on Electronic Structure Methods and Applications (ASESMA) series is a biannual event held on the African continent supported by the host African government as well as several international partners [2, 3]. This 2 weeks School provides intensive free training in the theory and hands-on experience and is highly recommended for graduate students and young faculty.

The largest provider of dedicated remote computational resources in science, technology and innovation is the Department of Science and Technology of the Republic of South Africa, through the Centre for High-Performance Computing in Cape Town. Depending on personal interest it is possible to join an existing research group. Kenya, being part of the global Square Kilometre Array (SKA) consisting of 9 African countries, has access to the computational resources at the CHPC [4]. The CHPC has research groups working on both fundamental and applied sciences. There are less than 10 Kenyan researchers who are registered as principal investigators at the CHPC but who can grant access to the resources provided one has a well defined research problem to investigate. There are global enterprises such Amazon and Microsoft Azure that are ready to get researchers and graduate students to test their computing resources in science, technology and innovation as well as other fields but have charges after a trial period.

It is possible that before 2008, there were graduate students and faculty engaged in computational modeling in fundamental and applied sciences in Kenya but the efforts were scattered. Beyond this period the initial institutional support from Moi University, the National Council for Science Technology and Innovation (NACOSTI, then National Council for Science and Technology), the International Centre for Theoretical Physics (ICTP, Trieste, Italy) enabled the first visibly coordinated research work in materials science research work through computational modeling. Later, support from University of Eldoret, ASESMA, the Emerging Nations Science Foundation (ENSF), the German Academic Exchange Service (DAAD), The Academy of Science of Developing Nations (TWAS), among other well wishers, enabled the growth of training and mentorship of graduate students as well as faculty. In May/June, the second ASESMA event in Africa was held in Kenya, in then Chepkoilel University College (now University of Eldoret) (See Figure 1 showing participants). Since then, materials science modeling in Kenya has been rated as only second to South Africa in African in terms of productivity in graduate student training and international peer reviewed publications [5].

Figure 1: Participants of 2nd ASESMA event in May/June 2012.

The initiatives in University of Eldoret received a direct support from the ENSF that was channeled to support meritorious undergraduate students in their final year between 2013 and 2017, graduate and postdoctoral students in a mentorship program aimed at preparation for graduate school and research. It is worth noting that just based on merit, the students who went through the program came all over the country (See table 1).

Table 1: Details of the mentees of the program and progression.

	Name (gender)	Entry level/ discipline	Area	Current status
1	Moro, Cecil	Undergrad /Physics	Comp. Mat. Sci	Phd/Physics – University of Pretoria Research Associate (CSIR, South Africa; HySA NWU, South Africa)
2	Mwonga, Patrick	Graduate	Comp. Mat. Sci	PhD/School of Physics Wits (Gauteng, South

		Msc/Physics		Africa)
3	Mutisya, Sylvia (F)	Undergrad /Physics	Comp. Mat. Sci	Phd/Physics - Brazil Postdoc/Physics Saclay, France
4.	Muchiri, Perpetua (F)	Undergrad /Physics	Comp. Mat. Sci	Msc/TU-K Graduate Assistant (TU-K)
5	Ochieng, Edmund	Undergrad /Computer Science	Cluster and Software support	System Admin at Rackspace Hosting (Texas, USA)
6	Mwalukuku, Valid	Undergrad /Chemistry	Comp. Mat. Sci	Msc/Chemistry Grenoble, France
7	Aradi, Emily (F)	Undergrad /Physics	Comp. Mat. Sci	Postdoc/Physics (UK)
8	Atambo Michael	Undergrad /Physics	Comp. Mat. Sci Cluster and Software support	PhD/Physics (Modena University, Italy) Lecturer, TU-K
9	Buko, Eric	Undergrad /Physics	Comp. Mat. Sci	PhD/Medical Physics (Texas, USA)
10	Ruggut, Elkana	Undergrad /Physics	Comp. Mat. Sci	PhD/School of Physics Wits (Gauteng, South Africa)
11	Korir, Kiptiemoi	Graduate PhD/Physics	Comp. Mat. Sci	Phd/Physics – Torino, Italy Lecturer, Moi University College, Busia
12	Meng'wa Victor	Graduate MSc/Physics	Comp. Mat. Sci	PhD/Physics UoE/OFID_ICTP/TU-K Lecturer, Alupe University

				College

Research activities in materials science at the national level are now supported by the Kenya Education Network (KENET) under the Computational Modeling and Materials Science (CMMS) special interest group. CMMS has over 70 research active Kenyan graduate students and faculty representing fundamental and applied sciences. KENET recently competitively awarded five mini grants to 5 Kenyans from public and private universities to carry out research on the areas of materials for green energy conversion and environmental safety.

3.0: Achievements and the need to focus on local problems

Following the growth of the group on Chepkoilel University College and later University of Eldoret, new groups have emerged in Masinde Muliro University of Science and Technology as well as Egerton University led by newly acquired PhDs who were part of the original vision. Through active collaborations, a group in Kabarak University is also now in its formative stages. It is estimated that through efforts to introduce high performance computing in materials science about 6 Phds and 15 Msc students have been trained since 2010 from University of Eldoret alone and much more at the national level.

For such knowledge and output to have an impact to the common citizens, a paradigm shift from publishing for its own sake or for promotions is needed. Graduate students and younger faculty should now go out to industry to seek current and emerging problems that have value to the country.

4.0: Conclusion and recommendations

Computational modeling in materials science is a research direction that can be used to investigate problems in fundamental and applied sciences giving high quality results. The largest informational impact on the use of the approach is realized when the approach is employed as a complementary check on experimental research work and also to provide predictive insights.

Institutions in Kenya, especially those previously shying away from fundamental and applied sciences, are encouraged to invest resources in this area in order to effectively use this approach for student and faculty training. There is an over reliance on the support from the Republic of South Africa for computational resources but it is my hope that the Government of Kenya will make an investment in local infrastructure for Kenyans undertaking research that will target projects of national strategic value using this approach.

collaborators in University of Eldoret (Nicholas Makau), South Africa (Daniel Joubert, Cecil Ouma), Japan (Ryo Maezono and Kenta Hongo) and Europe (Nicola Seriani, Sandro Scandolo, Mark Casida) is highly appreciated.

References

1. The Kenya Education Network, Nairobi - https://www.kenet.or.ke/

2. African School on Electronic Structure Methods and Applications https://sites.google.com/site/asesmasite/

3. George Amolo, Nithaya Chetty, Ali Hassanali, Daniel Joubert, Richard Martin and Sandro Scandolo, *Growing materials science in Africa – The case of the African School on Electronic Structure Methods and Applications (ASESMA), MRS Advances, Cambridge University Press; DOI: 10.1557/adv.2018.185 (2018).*

4. CHPC – Centre for High Performance Computing - https://www.chpc.ac.za/

5. George Amolo, *The Growth of High Performance Computing in Africa*: *Computers in Science and Engineering (CISE)* (www.computer.org/cise), IEEE Publication (2018).

Pressure Dependency of Elasticity in α-TiZr Shape Memory Alloys

Job W. Wafula,[1,2] George S. Manyali,[2] John W. Makokha,[1] James Sifuna [2,3,4]

[1]Materials Science, Department of Science, Technology and Engineering,
Kibabii University, 1699-50200, Bungoma, Kenya,

[2]Computational and Theoretical physics group (CTheP), Department of Physics,
Masinde Muliro University of Science and Technology, 190-50100, Kakamega, Kenya,

[3]Materials Modeling Group, Department of Physics and Space Sciences,
The Technical University of Kenya, 52428-00200, Nairobi, Kenya

[4]Department of Natural sciences,
The Catholic University of Eastern Africa, 62157-00200, Nairobi, Kenya

Tel: + 254715158787, + 254728317456, +254721825520, +254725499073
Email: jobwafula691@gmail.com, georgemanyali@mail.com, makokhajw@gmail.com,
sifunajames@gmail.com.

Abstract:

Shape memory alloys are a group of materials with two noteworthy properties; shape memory effects and superelasticity thus they have attracted a number of industrial applications. Elasticity is the ability of a material to resume its normal shape after being stretched or compressed when the elastic limit is not exceeded. Titanium Nickel, copper-based and iron-based shape memory alloys are mostly applied in constructions sector but they face challenges of pressure dependency. To provide a solution, we investigated the pressure dependency of elasticity in α-TiZr shape memory alloy. Elastic constants, bulk modulus, Young modulus, shear modulus and Poisson's ratio of α-TiZr shape memory alloy were calculated at different pressure (0-10GPa) using Quantum ESPRESSO code with post-processing of the data done using Thermo_pw code. Projector augmented wave pseudo-potential with Generalized Gradient Approximations (GGA) within Perdew, Burke, and Ernzerhof (PBE) exchange-correlation functional was applied in this study. Elastic constants; C_{11}, C_{12}, C_{13} C_{33}, and C_{66} of α-TiZr shape memory alloy increase with pressure monotonically except C_{44} which slightly decrease linearly. Furthermore, Bulk modulus, Young's modulus shear modulus and Poison's ratio were also observed to increase with external pressure. This indicates that elasticity of α-TiZr shape memory alloy is improved when external force is exerted on crystal. The study of pressure dependency of elasticity in α-TiZr shape memory alloy provides information which may lead to adoption of this alloy in construction of intelligent reinforced concrete (IRC).

Keywords: α-TiZr, Elasticity, Density functional theory.

1. Introduction

The Shape memory alloys (SMAs) belong to a class of shape memory materials (SMMs), which have the ability to 'memorise' or retain their previous form when subjected to certain stimulus such as thermo-mechanical (Jani *et al*., 2014). The Titanium Zirconium (TiZr) shape memory alloy undergoes a reversible martensitic transformation from the hexagonal 'α' martensite to the cubic '*β*' austenite at the start temperature (*As*) of 871 K and the martensitic transformation with the start temperature (*Ms*) of 813 K (Li *et al*., 2011). Shape memory alloys have been fully utilized in a number of industries due to their benefits of superelasticity, shape memory effect and high damping

Available online http://ir.kabarak.ac.ke/handle/123456789/1

properties. Titanium Nickel, copper-based and Iron-based shape SMAs are among materials so far used in the construction of concrete of buildings and bridges. However, the alloys mentioned above have not been fully adopted in the construction sector due to limitations of temperature (Chang *et al*., 2016) and pressure dependent behaviors. This is besides their low martensitic transformation temperatures (Baloyi *et al*., 2018). Variation of external pressure can cause cracks on buildings and bridges making them unsafe for use. SMA wires were introduced in civil structures as Intelligent Reinforced Concrete (IRC) because they can sense cracks and reduce large scale sized cracks. Therefore, there is need for building and bridge materials that can dissipate energy with minimum structural damage and return to their initial position as a result of changes in temperatures and pressures (Chancellor *et al*., 2014). The first application of SMAs in concrete structure was on a highway bridge in Michigan and from that innovative project that helped to close the cracks it was realized that the behavior of SMAs was to be under different working temperatures (Soroushian *et al*., 2015). The elastic properties of hexagonal crystal of TiZr SMA under the external pressure between 0 GPa to 10 GPa at constant temperature 0 K were investigated by the density functional theory method (DFT). This paper is organized as follows; in Section 2, the computation details are given. The results and discussion are presented in section 3. Finally, a conclusion of our results is shown in section 4.

2. Computational details

All the calculations were performed by Density Functional Theory (DFT) (Kohn *et al*., 1965) implemented in Quantum ESPRESSO codes (Giannozi *et al*., 2017) using Thermo_pw code as post-processing tool (Corso *et al*., 2016). The ion–electron interaction was described by the Projector augmented wave (PAW) method and exchange-correlation functional is treated within the Perdew, Burke, and Ernzerhof (PBE) of generalized gradient approximation (GGA) (Perdew *et al*., 1996). The valence electron configurations for Ti and Zr are $3d^34s^1$ and $4d^35s^1$. The plane wave cut-off energy was set as 50 Ry since it was sufficient to converge the total energy of α-TiZr Shape Memory Alloy. K-point meshes of $16\times16\times12$ for the Brillouin zone was sampled based on Monkhorst-Pack scheme (Monkhorst *et al*., 1976). Before calculating the elastic constants of the TiZr alloy at a given pressure P, the unit cell of the compound at the corresponding pressure was relaxed until the atomic forces were less than 0.001 eV/Å and stress of less than 0.02 kbar.

3. Results and discussions

3.1 Structural properties

The unit cell of α-TiZr shape memory alloy in α structure consists of two atoms with space group P $\bar{6}$m2 (187) as shown in figure 1. Since the structure is hexagonal therefore lattice parameters; a=b≠c with bond angles $\alpha=\beta=90^0$ and $\gamma=120^0$ and the bond lengths under different pressure are presented in table 1. The α-TiZr shape memory alloy has sigma covalent bond with the mass of unit cell of 139.0910 a.m.u. The calculated values for lattice constants and bulk modulus both from Equation of state (EOS) and Thermo_pw tool presented in Table I are in good agreement with previous experimental and theoretical data at 0GPa.
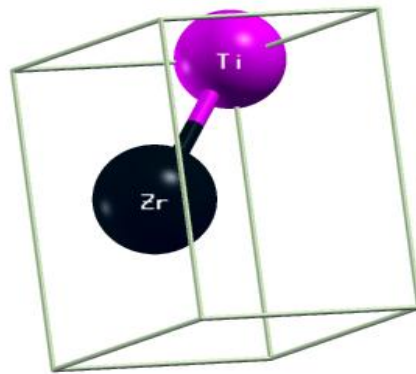
Figure 1. (Color online) The unit cell of α-TiZr with two atoms at Zr (0.333333 0.666667 0.250000) and Ti (0.666667 0.333333 0.750000) positions.

Table 1. Indicating the calculated values of the lattice parameter a, Bulk modulus B_0, the first pressure derivative of the Bulk modulus B', Bond length (Å) and the densities at different pressures in comparison with experimental studies and other theoretical work

Pressure (GPa)		Reference	a (Å)	B_0 (GPa)	B'_o	Bond length(Å)	Density (g/cm^3)
0	EOS	This work	3.08	97.73	3.42		5.62
0			3.07			3.07	5.65
2			3.05			3.05	5.76
4			3.03			3.03	5.87
6	Thermo_pw	This work	3.01			3.02	5.93
8			2.99			3.00	6.07
10			2.97			2.99	6.16
0	Expt	(Bashkin *et al.,* 2003)	3.10	148.00	3.80		
		(Li *et al.,* 2011)	3.12				
0	Other studies	(Wang *et al.,* 2011)	3.11	97.80	3.47		
		(ikehata *et al.,* 2004)	3.11				
		(Ho *et al.,* 2008)	3.06				

The bulk modulus and its pressure derivative were calculated by minimizing the total energy for different values of the lattice constant according to the third-order Birch–Murnaghan equation of state (EOS) (Birch, 1947).

$$P(V) = \frac{3B_0}{2} \left[\left(\frac{V_0}{V}\right)^{\frac{2}{3}} - \left(\frac{V_0}{V}\right)^{\frac{5}{3}} \right] \left\{ 1 + \frac{3}{4}(B_0' - 4) \left[\left(\frac{V_0}{V}\right)^{\frac{2}{3}} - 1 \right] \right\} \tag{1}$$
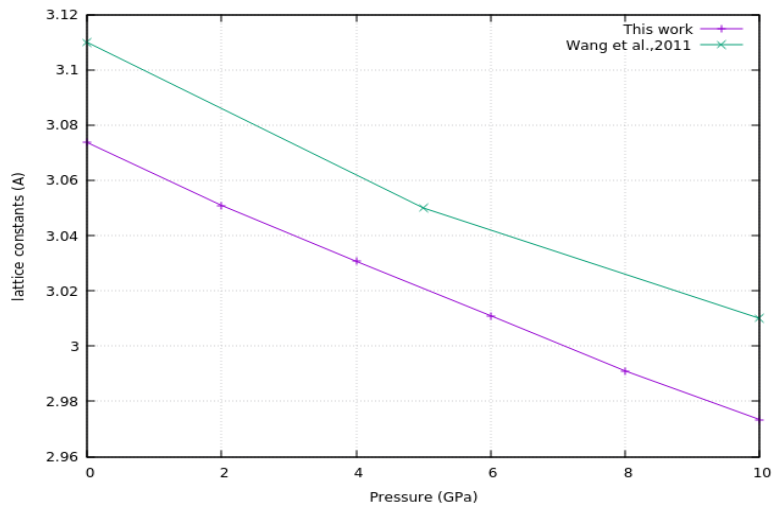

Figure 2. Calculated lattice parameters of α-TiZr Shape Memory Alloy under pressure in comparison with other theoretical data of Wang et al.
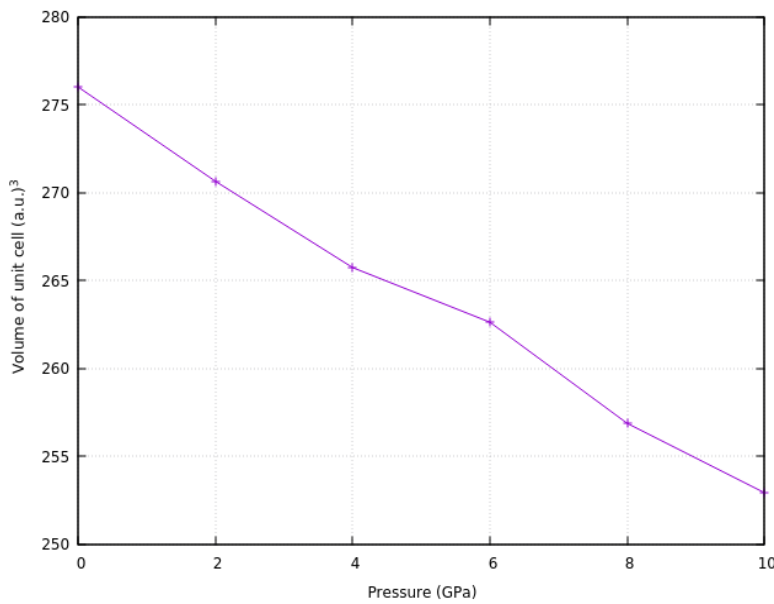

Figure 3. Shows the variation of volume of unit cell (a.u)^3 of α TiZr Shape memory alloy under external pressure up to 10GPa.
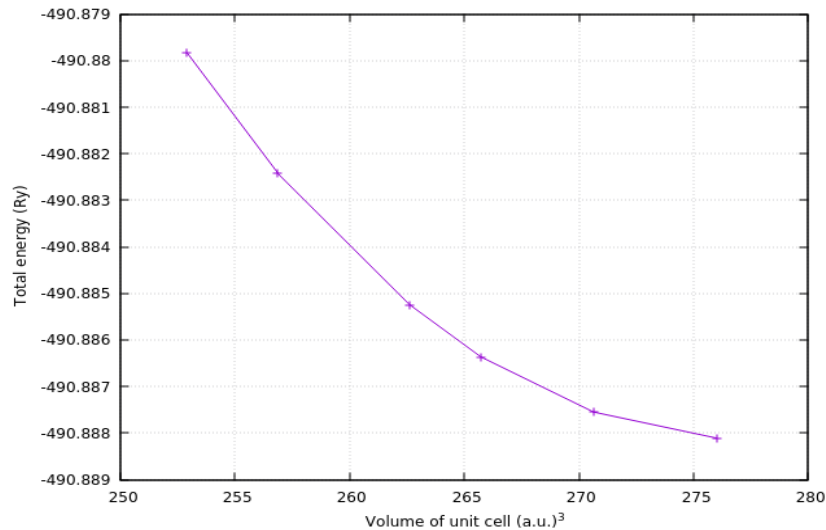
Figure 4. Indicates the variation of total energy (Ry) of α TiZr SMA with the volume of the unit cell under pressure up to 10GPa.

It is clear that there exists an inverse relationship between compression of a material and its lattice parameter. From the figure 3, we observed volume of unit cell $(a.u)^3$ decreases as the external pressure is applied and the smaller the lattice parameter, the smaller the volume and hence a large bulk modulus (Sifuna *et al*., 2017). This implies that bulk materials have a high resistance against volume deformation. In Figure 2, variations of the lattice parameters of α-TiZr Shape Memory Alloy with pressure are presented to investigate the influence of external pressure on the crystal structure of α-TiZr Shape Memory Alloy. It is observed that the lattice constants decrease with increase in external pressure. This is due to reduction of distance between the atoms as a result of pressure increase hence the repulsive interaction between atoms strengthens, leading to the difficulty to compress the crystal (Zhao *et al*., 2015). Figure 4 shows minimum total energy of α-TiZr Shape memory alloy at different pressure, we observe that minimum energy of the ground state increases with pressure. This is because when external pressure is applied to unit cell of α-TiZr Shape memory alloy, the bond length shortens thus the strength of covalent bond increases. The stronger the covalent bond the higher the minimum energy for the ground state.

3.2 Mechanical properties

3.2.1 Elastic properties

When a crystal is subjected to deformation of a certain magnitude of strain (σ), the restoring forces appear to bring it to the equilibrium state (Manyali, 2018). These restoring forces can be described by the stress tensor. For a small strain (ε) deforming a material determined by Hooke's law; (Landau *et al*., 1959)

$$\sigma_{ij} = C_{ijkl}\varepsilon_{ij} \tag{2}$$

C_{ijkl} represents the elastic constants. Hence, the elastic matrix of hexagonal system is given as:

$$
\begin{pmatrix} \sigma_1 \\ \sigma_2 \\ \sigma_3 \\ \tau_1 \\ \tau_2 \\ \tau_3 \end{pmatrix}
\begin{pmatrix}
C_{11} & C_{12} & C_{13} & & & \\
 & C_{11} & C_{13} & & & \\
 & & C_{33} & & & \\
 & & & C_{44} & & \\
 & & & & C_{55} & \\
 & & & & & C_{66}
\end{pmatrix}
\begin{pmatrix} \varepsilon_1 \\ \varepsilon_2 \\ \varepsilon_3 \\ \gamma_1 \\ \gamma_2 \\ \gamma_3 \end{pmatrix}
\tag{3}
$$

where $\sigma_i, \tau_i, \varepsilon_i, \gamma_i$ are normal stress, shear stress, the corresponding normal strain and shearing strain respectively. In the current work elastic constants that were calculated for α-TiZr shape memory alloy under pressure up to 10GPa are presented in the table 2. The elastic properties such as the bulk modulus B, shear modulus G, Young's modulus E and Poisson's ratio are directly calculated by the Voigt-Reuss-Hill method (Hill, 1952). The results are listed in Table 2 and shown in Figure 6 and 7.

$$
B_V = \frac{2C_{11} + 2C_{12} + 4C_{13} + C_{33}}{9} \tag{4}
$$

$$
B_R = \frac{(C_{11}+C_{12})C_{33} - 2C_{13}^2}{C_{11}+C_{12} - 4C_{13} + 2C_{33}} \tag{5}
$$

The Voigt average shear modulus is determined by the equation; (Voigt, 1928)

$$
G_V = \frac{C_{11} + C_{12} - 4C_{13} + 2C_{33} + 12C_{44} + 12C_{66}}{30} \tag{6}
$$

While Reuss average the shear modulus *(G)* is be given by the equation (Reuss, 1929)

$$
G_R = \frac{5\left[(C_{11}+C_{12})C_{33} - 2C_{13}^2\right]C_{44}C_{66}}{6B_V C_{44}C_{66} + 2\left[(C_{11}+C_{12})C_{33} - 2C_{13}^2\right](C_{44}+C_{66})} \tag{7}
$$

From the Voigt-Reuss-Hill average, bulk modulus and shear modulus is expressed as;

$$
B = \frac{B_V + B_R}{2} \tag{8}
$$

$$
G = \frac{G_V + G_R}{2} \tag{9}
$$

A compound with a larger shear modulus implies its higher resistance to reversible deformations (Chen *et al*., 2014). Once the bulk and shear moduli are determined, Young's modulus (E) and Poisson's ratio ($\mathcal{V}$) are determined as shown below; (Greaves *et al*., 2011)

$$
E = \frac{9BG}{3B + G} \tag{10}
$$

$$
V = \frac{3B - 2G}{2(3B+G)} \tag{11}
$$

Vicker's hardness H_v is associated with elastic properties of alloys. It denotes the resistance to elastic and plastic deformations when a force is loaded (Chang *et al*., 2018). Hardness can be predicted by the following equation; (Tian *et al*., 2012)

$$
H_v = 0.92(G/B)^{1.137} G^{0.708} \tag{12}
$$

3.2.2 Debye temperature θ_D and sound velocity V_m

The Debye temperature of a material is parameter associated with lattice vibrations used to describe the structural stability and the strength of bonds. It depends on the elastic constants and it is estimated from the average sound velocity V_m as shown; (Anderson, 1963)

$$\Theta_D = \frac{h}{k_B} \left(\frac{3n}{4\Pi V_a}\right)^{\frac{1}{3}} V_m \tag{13}$$

Where h is Plank's constant, k_B is Boltzmann's constant, n is number of atoms per formula unit and V_a is atomic volume.

The average sound velocity V_m ;

$$V_m = \left[\frac{1}{3}\left(\frac{1}{V_l^3} + \frac{2}{V_t^3}\right)\right]^{\frac{-1}{3}} \tag{14}$$

V_l is the longitudinal sound velocity and V_t is the transverse sound velocity of an isotropic aggregate determined as shown below;

$$V_l = \left(\frac{3B+4G}{3\rho}\right)^{\frac{1}{2}} \tag{15}$$

$$V_t = \left(\frac{G}{\rho}\right)^{\frac{1}{2}} \tag{16}$$

B is bulk modulus; G is the shear modulus and ρ is the density. By using the VRH method, average sound velocity and Debye temperatures with pressure range from 0 to 10 GPa is calculated and the results are listed in table 2.

Table 2. Mechanical properties and elastic constants for α-TiZr shape memory alloy under pressure up 10GP.

|		Pressure (GPa)						Expt studies	Other studies
		0	2	4	6	8	10	0 (GPa)	0 (GPa)
C_{11} (GPa)		143.78	153.12	161.25	168.82	178.52	185.63	137.70	145.10
C_{12} (GPa)		64.55	69.46	74.12	75.09	83.35	87.14	75.30	72.50
C_{13} (GPa)		81.24	87.99	94.35	98.15	107.73	113.55	67.80	70.90
C_{33} (GPa)		144.30	155.69	165.84	169.86	189.29	194.14	164.00	169.00
C_{44} (GPa)		30.34	30.44	30.34	30.02	29.40	28.63	30.00	30.00
C_{66} (GPa)		39.61	41.83	43.56	46.86	47.58	49.24		
Θ_D (K)		297.30	301.57	304.21	307.47	308.18	308.33		
V- R-H (GPa)	B	98.4	105.60	112.30	116.36	126.21	132.00		
	E	90.83	93.46	95.97	98.65	100.30	101.28		
	G	33.73	34.55	35.34	36.30	36.67	36.91		
	V	0.346	0.352	0.357	0.358	0.367	0.372		
V_m(m/s)		2730.76	2751.91	2759.08	2777.68	2763.63	2750.76		
B/G		2.91	3.05	3.17	3.20	3.44	3.57		
H_V (GPa)		3.10	3.44	3.56	3.64	3.77	3.84		
Ref		This work						(ikehata *et al.,* 2004)	(Wang *et al.,* 2011)
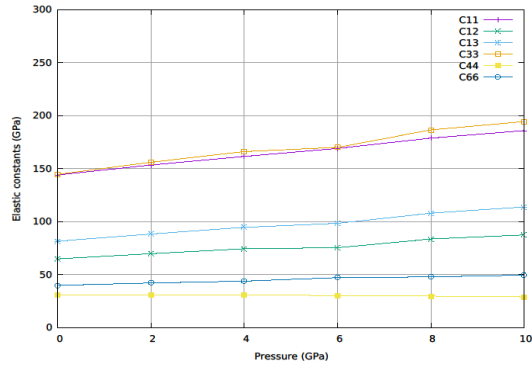
Figure 5. (Color online) Shows the pressure dependence of elastic constants in of α-TiZr SMA.
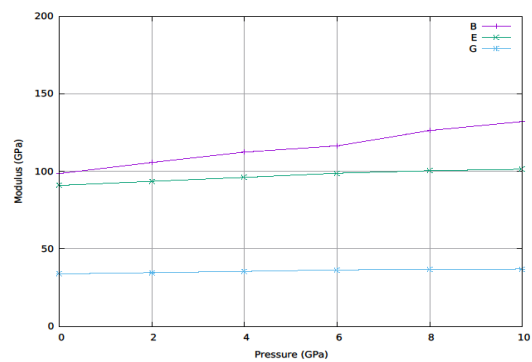
Figure 6. (Color online) Shows Bulk modulus, Young's modulus and shear modulus of α-TiZr memory shape alloy under pressure up to 10GPa.

Figure 7. (Color online) Shows the poison's ratios and Pugh's ratios of α-TiZr SMA under pressure up to 10 GPa.

Figure 8. (Color online) Shows the Debye

temperatures of α-TiZr SMA under varying pressure up to 10GPa.

Figure 9. Hardness of α-TiZr memory alloy under pressure up to 10GPa

Figure 10. Shows the average Debye sound velocity of α-TiZr shape memory alloy under increasing pressure up to 10GPa.

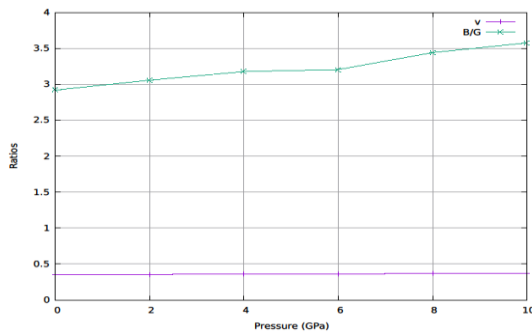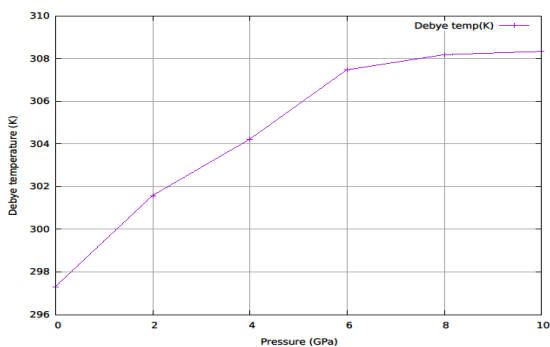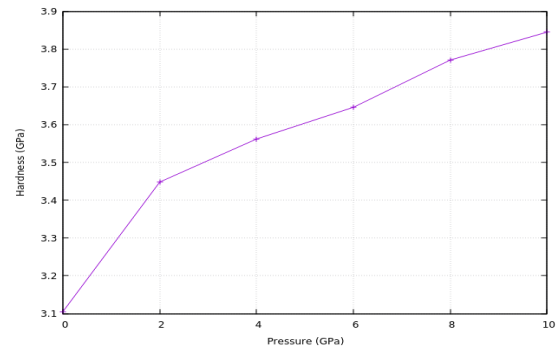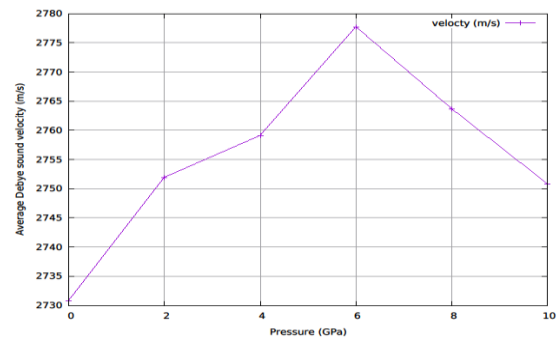The stability in the hexagonal is based on the following conditions; (Born *et al.*, 1954)

$$C_{11} > 0; 2C_{11}^2 < C_{33}(C_{11} + C_{11}); C_{11} > 0; C_{66} > 0 \qquad (17)$$

Therefore, α-TiZr shape memory alloy is mechanically stable under external pressures between 0GPa to 10GP.

3.2.1 Pressure-Dependency of Elasticity

The information about elasticity under pressure helps us to understand the deformation behavior of a solid in response to external forces. In addition, the information provides a deeper insight into macroscopic mechanical behavior and estimate the hardness of materials (Chang *et al.*, 2018). The calculated elastic constants are in good agreement with other studies as shown in table 2. The elastic constants C_{11} and C_{33} represent the elasticity in length. The other constants C_{12} and C_{44} are shear constants and are associated with the elasticity in shape. (Liu *et al.*, 2012) It is evident that the elastic constants C_{11}, C_{12}, C_{13}, C_{33} and C_{66} of α-TiZr SMA increase linearly with pressure due to the denser packing of the atoms brought about by compression. The constants C_{11} and C_{33} are more sensitive to pressure compared to C_{12} and C_{13}, while C_{44} decreases slightly with pressure. We also noted that the elastic constant C_{11} is slightly smaller than C_{33} at the same pressure, therefore, it is easier to compress along the x-direction than along the z-direction.

Both Poisson's ratio ($\mathcal{V}$) and Pugh's ratio (B⁄G) are used to determine if the compounds are ductile or brittle for instance if *v*>0.26 (Greaves *et al.*, 2011) or B⁄G>1.75 (Pugh's 1954) indicates that the crystal structure is ductile, otherwise brittle. From the Table 2 we realized that Pugh's ratios of α-TiZr shape memory alloy are greater than 1.75, thus this alloy is ductile. The ratios increase with pressure due to the strengthening of covalent bond, which suggests that higher pressure can improve the ductility as shown in Figure7. Poisson's ratio measures the stability of the crystal against shear, and the larger the Poisson's ratio, the better the plasticity (Cao *et al.*, 2013). It is clear that the Poisson's ratio of α-TiZr shape memory alloy increases with pressure. Therefore, presence of an external pressure improves the plasticity α-TiZr shape memory alloy.

The values of bulk modulus from the Figure 6 are much greater than that of shear modulus, thus α-TiZr alloy tends to resist volume change better than shape change (Pugh, 1954). Young's modulus E shows the stiffness of a solid, for instance the materials with larger E are stiffer (Liu *et al.*, 2013). Therefore, α-TiZr shape memory alloy becomes much stiffer when pressure increases. Moreover, it can be seen that values of B, G and E increase with pressure. This is because applied external pressure reduces the bond length hence the bond between Ti and Zr becomes stronger.

3.2.2 Pressure dependency of Vicker's Hardness in α-TiZr SMA

Our calculated value of Vicker's hardness indicated in table 2 lie between 3-4GPa suggesting that the α-TiZr SMA is soft. The Vicker's hardness increases with pressure as shown in Figure 9 due to increase in the strength of covalent bonds with external pressure. It is also noted that the shear modulus of materials plays a more important role in hardness than the bulk modulus of materials.

3.2.3 Pressure dependency of Debye temperature and sound velocity in α-TiZr SMA

Debye temperature is the temperature at which almost all modes of vibrations in a solid are excited (Bhatli *et al*., 1986). We found out that the Debye temperature of α-TiZr shape memory alloy increases with pressure which implies that the rigidity of the α-TiZr shape memory alloy increases with pressure as shown in Figure 8. Debye temperature is used to describe the strength of the covalent bond for instance the larger the Debye temperature the stronger the covalent bond (Liu *et al*., 2013). Therefore, with increase in external pressure, the covalent bonds of α-TiZr shape memory alloy become stronger.

Average sound velocity in α-TiZr SMA increase nonlinearly with pressure up to 6GPa and drops monotonically with further increase in pressure as shown in table 2 and Figure 10. Vibration frequency increases with pressure however, when external pressure increases beyond 6GPa, frequency decreases. This indicates that the bonds between the Ti and Zr atoms are strengthened as the distance between these two atoms becomes shorter with increasing pressure. The average sound velocity is determined from longitudinal sound velocity and transverse sound velocity which are related to elastic constants C_{11} and C_{44} using equations; $V_l = \sqrt{C_{11}}/\rho$ and $V_t = \sqrt{C_{44}}/\rho$ respectively. Longitudinal wave of compression depends on C_{11} while transverse wave is controlled by C_{44}. Therefore, transverse sound velocity of α-TiZr shape memory alloy increases while longitudinal sound velocity decreases under pressure. Normally $C_{11} > C_{44}$ hence $V_l > V_t$ (Anderson, 1963).

Conclusions

In this paper, we have investigated the elasticity of α-TiZr shape memory alloy under various pressures up to 10GPa at a constant temperature 0K using Density Functional Theory. In our conclusion we realized the following; the obtained lattice constant of of α-TiZr shape memory alloy (3.07 Å) at 0 GPa is in good agreement with experimental and other theoretical values. Secondly, calculated elastic constants satisfies Born's stability criterion, therefore, α-TiZr Shape Memory Alloy is mechanically stable under pressure between 0GPa to 10GPa. Generally, elasticity of α-TiZr Shape Memory Alloy improves with increase in external pressure. In our research we focused on pressure dependency of elasticity in the α-TiZr Shape Memory Alloy at constant temperature however, temperature change may also cause cracks in buildings and bridges because of expansion and contraction. Therefore, further studies are necessary to understand the temperature dependent behaviors of α-TiZr shape memory alloy.

Acknowledgement

References

Anderson O.L., J. (1963). Phys. Chem. *Solids, 24,* 909.

Baloyi, M. E., Modiba, R., Chauke, H.R., and Ngoepe, P.E., (2018) IOP Conf. Ser.: *Mater. Sci. Eng.* 430 01202.

Bhatli, S. S., and Singh, S. T., (1986). J. Pure Appl. *Ultrasound. 8,* 1019 .

Bashkin, I.O., Fedotov, V.K., Nefedova, M.V., Tissen, V.G., Ponyatovsky, E.G., Schiwek, A., Holzapfel, W.B., (2003) Phys. *Rev. B* (68) 054401.

Birch, F., (1947). Phys. *Rev*. 71:809.

Born, M., and Kun, H., (1954). *Dynamical theory of crys-tal*, Clarendon press.

Cao, Y. Zhu, J.C. Liu, Y. Nong, Z.S. Lai, Z.H., (2013). Comp. Mater. *Sci*. 69 40.

Chancellor, N.B., Eatherton, M.R., Roke, D.A., and Akbaş, T., (2014). *Self-centering seismic lateral force resisting systems: High performance structures for the city of tomorrow. Buildings 4(*3): 520–548.

Chang, J., Zhou, X., Liu, K., Ge, N., (2018). R. Soc. open sci. *Structural, elastic, mechanical and thermodynamic properties of HfB4 under high pressure*. 5: 180701.

Chang, W. and Araki, Y. (2016). civil Engineering. *Use of shape-memory alloys in construction: a critical review;* (169): issue (CE2).

Chen, D.; Chen, Z.; Wu, Y.; Wang, M.; Ma, N.; Wang, H. (2014). Comput. Mater. Sci. *First-principles investigation of mechanical, electronic and optical properties of Al_3Sc intermetallic compound under pressure.* (91): 165–172.

Corso, D.A. (2016) J. Phys.: *Condens. Matter, 28,* 07540.

Giannozzi, P., Baroni, S., Bonini, N., Calandra, M., Car, R., Cavazzoni, C., Ceresoli, D., Chiarotti, G., Cococcioni, G., Dabo, I., *et al*., (2017). Journal of Physics: *Condensed Matter, 29,* 465901.

Greaves, G.N.; Greer, A.L.; Lakes, R.S.; Rouxel, T. (2011). Nat. Mater. *Poisson's ratio and modern materials*.10, 823–837. K, 1954.

Hill, R., (1952). Phys. Soc. Lond. Sect. *The Elastic Behaviour of a Crystalline Aggregate*. A, (65) 349–354

Ho, W.F. Chen, S.C. Wu, H.C. Hsu, (2008) J. Mater. *Med. 19,* 3179

Ikehata, H., Nagasako, N., Furuta, T., Fukumoto, A., Miwa, K., Saito, T., (2004). Phys. *Rev. B* (70) 174113.

Kohn, W., Sham, L. J., (1965). Phys. *Rev. 140* (4A) A1133–A1138.

Landau, L. D., and Lifshits, E. M. (1959). *Theory of elasticity (Translated from the Russian by J.B. Sykes and W.H. Reid)*. Addison-Wesley physics books. London, Pergamon Press; Reading, Mass., Addison-Wesley Pub. Co.

Li, Y., Cui, Y., Zhang, F and Xu, H. (2011). */ Scripta Materialia* (64): 584–587.

Liu, Y., Hu, W.C., Li, D.J., Zeng, X.Q., Xu, C.S., (2013). *Phys. Scr.* 88, 045302.

Liu, Y., Hu, W.C., Li, D.J., Zeng, X.Q., Xu, C.S., Yang, X.J. (2012). *Intermetallic,* 31, 257-263.

Manyali G.S., (2018) *High bulk modulus but low Vicker's hardness: A DFT study of mechanical properties of hcp rhenium, arXiv:* 1905.04526v1.

McNaught, A.D.; Wilkinson, A. (1997) *Compendium of Chemical Terminology.* In The Gold Book, 2nd ed.; Blackwell Scientific Publications: Oxford, UK,Volume 2, pp. 12–14, ISBN 0-86542-684-8.

Jani, M.J. Leary, M. Subic, A. Gibson, M.A. (2014). / *Materials and Design 56*, 1078–1113.

Monkhorst, H.J., Pack, J.D., (1976). *Phys. Rev. B* 13, 5188.

Perdew, J.P. Burke, K. Ernzerhof, M. (1996). Phys. Rev. *Lett. 77*, 3865.

Pugh, S.F., (1954). Philos. Mag. *Relations between the elastic moduli and the plastic properties of polycrystalline pure metals*, *XCII* 45, 823–843.

Reuss, A., (1929). Angew. Math. Mech. *Calculation of the flow limits of mixed crystals on the basis of the plasticity of monocrystals, Z,* (9): 49–58.

Sifuna, J., Manyali, G.S., Sakwa, T., Kitui, M.M., (2017) *Structural and Mechanical Properties of Bulk Scandium Trifluoride Investigated by First-Principles Calculations*; (4) 2; ISSN: 2458-9403

Soroushian, P., Ostowari, K., Nossoni, A and Chowdhury, H., (2015). Transportation Research Record. *Repair and strengthening of concrete structures through application of corrective posttensioning forces with shape-memory alloys.* 1770: 20–26. uly, Cambridge, UK.

Tian, Y.; Xu, B.; Zhao, Z. (2012). Int. J. Refract. Met. Hard Mater. *Microscopic theory of hardness and design of novel superhard crystals*, *33*, 93–106.

Voigt, W. (1928) Lehrbuchde Kristall. *physik*; B.G. Teubner: Leipzig/Berlin, Germany.

Wang, B.T., Li, W.D. and Zhang, P (2011). *First-principles calculations of phase transition, elasticity, and thermodynamic properties for TiZr alloy*, Beijing. China.

Zhao, Y., Qi, L., Jin, Y., Wang, K., Tian, J. and Han, P., (2015). */ Journal of Alloys and Compounds* 647, 1104e111.

Effects of solvent polarity on the absorption and fluorescence spectra of 3-cyano-7-hydroxy-4-methylcoumarin: Determination of the dipole moments and application to epifluorescence microscopy

Kebenei, J. Sellah[a] and Akumu E. Otieno[a*]

[a]Department of Physical and Biological Sciences. Kabarak University.
Private bag-20157
Kabarak
*Corresponding author: oakumu@kabarak.ac.ke

Abstract

The Absorption and fluorescence emission spectra of 3-cyano-7-hydroxy-4-methylcoumarin (3C7H4M) were studied in solvents of different dielectric constant ε and refractive index n. Experimental ground and excited state dipole moments were established by means of solvatochromic shift method. Both the ground state and excited state dipole moments were established. Results revealed that the excited state dipole moments of 3C7H4M were higher than those of the ground state. Further it is evident from these results that, the changes in the dipole moments on electronic excitation are small. Since 3C7H4M is more polar in its excited state, polar solvents were chosen in epifluorescence study. The epifluorescent microscopy images of a plant cell stained by 3C7H4M in various polar solvents compared with Iodine are hereby reported.

Keywords: 3-cyano-7-hydroxy-4-, *dipole moments, epifluorescence, spectral shifts*

Introduction

Photochemical studies on molecules typically requires knowledge of spectral features(Taniguchi & Lindsey, 2018). Fluorophores have unique electronic and photonic properties such as, relatively shorter lifetime, high quantum yield and broad spectral band width which can be applied in numerous technological applications (Raikar et al., 2006).

Coumarin dyes are well known photosensitizing agents(Zhang, Zhang, & Xia, 2008). They can be used in photobiology because of their photodynamic actions. They are known to show interesting photochemical behavior, particularly dimerization in polar and non-polar solvents (Perez-Rodriguez, Aguilera, & Figueroa, 2003).

The widespread occurrence of coumarin derivatives in nature (Kirsch, Abdelwahab, & Chaimbault, 2016) and their variety of applications have made their study very interesting. Dipole moments of short-lived species are of significant interest as they provide both electronic and geometrical structure information of the dye (Sharma, Jain, & Rastogi, 2007). The information on dipole moments of electronically excited species is helpful in the designing non-linear optical materials and understanding their photochemical transformations (Patil, Melavanki, Kapatkar, Ayachit, & Saravanan, 2011). Fluorescence experimental data on excited states are handy in the parameterization of semi-empirical quantum chemical procedures for these states (Grotkopp, Mayer, & Müller, 2018).

Determination of the ground and excited state dipole moments of dye molecules is important, because the values so obtained provide information about the change in electronic distribution upon excitation(Biradar, Siddlingeshwar, & Hanagodimath, 2008) The most popular technique for the determination of excited state dipole moments is based on the Lippert–Mataga equation (Vequi-Suplicy, Coutinho, & Lamy, 2014) in which absorption and fluorescence shifts described by dielectric constant ε and refractive index n are followed using the solvent polarity.

In this paper we report determination of dipole moments using different solvent parameters, refractive index, dielectric constant ε, spectral parameters like stokes shift. We have calculated

the ground and excited state dipole moments of 3C7H4M dye by solvent perturbation method based on absorption and fluorescence shift in solvents with varied polarities.

Theoretical

From the quantum mechanical perturbation theory of absorption($\tilde{V}_a$) and fluorescence ($\tilde{V}_f$) band shifts in different solvent permittivity (ε) and refractive index (η), the following equations (Nagaraja, Patil, Kusanur, Patil, & Melavanki, 2012), were used to determine both ground state and excited state dipole moments of the sample dye;

$$\tilde{V}_a - \tilde{V}_f = m_1 f(\varepsilon, n) + constant$$

and

$$\tilde{V}_a + \tilde{V}_f = m_2[f(\varepsilon, n) + 2g(n)] + constant$$

the solvent polarity parameter is given by;

$$f(\varepsilon, n) = \frac{2n^2 + 1}{n^2 + 2}[\frac{\varepsilon - 1}{\varepsilon + 2} - \frac{n^2 - 1}{n^2 + 2}]$$

and

$$g(n) = \frac{3}{2}[\frac{n^4 - 1}{(n^n + 2)^2}]$$

with

$$m_1 = \frac{2(\mu_e - \mu_g)}{hca^3} \dots\dots\dots\dots\dots\dots(1)$$

and

$$m_2 = \frac{2(\mu_e^2 - \mu_g^2)}{hca^3} \dots\dots\dots\dots\dots(2)$$

Where h is the Planck's constant, c is the velocity of light in vacuum. μ_g and μ_e are the dipole moments in the ground and exacted states respectively which are calculated as follows;

$$\mu_g = \frac{m_2 - m_1}{2}[\frac{hca^3}{2m_1}]^{\frac{1}{2}} \dots\dots\dots\dots\dots(3)$$

$$\mu_e = \frac{m_2 + m_1}{2}[\frac{hca^3}{2m_1}]^{\frac{1}{2}} \dots\dots\dots\dots\dots (4)$$

The Onsager radius "a" of the solute molecule can be evaluated by using Edward's atomic increment method (Kadolkar, Patil, Kariduraganavar, & Inamdar, 2019) as follows;

$$a = [\frac{3M}{4\pi\delta N_A}]^{\frac{1}{3}}$$

Experimental

3C7H4M was purchased from Aldrich Chemical Co. and was used without further purification. The molecular structure of 3C7H4M is as given in Fig. 1. All the solvents used viz., methanol, ethanol, ethyl acetate, THF, and *n*-hexane, were of spectroscopic grade. Electronic absorption spectra were recorded on an Mrc UV-11 Model UV–Vis spectrophotometer. Fluorescence spectra were taken by using a Biobase-BKF93 Model F2000 fluorospectrometer at room temperature. Refractive index was measured using ATAGO model pocket refractometer PAL-1. Staining solutions of 3-cyano-7-hydroxy-4-methylcoumarin in water and methanol were prepared by dissolving 0.1 mg of the dye in 100 mL of distilled water (1 ppm). Iodine was prepared as per standard laboratory procedure. Each mixture was stirred for dye solubilization and filtered before use.
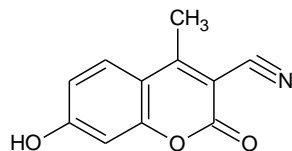
Fig.1. structure of 3-cyano-7-hydroxy-4-methylcoumarin

Results and discussion

Absorption and fluorescence emission spectra of 3-cyano-7-hydroxy-4-methylcoumarin (3C7H4M) and was recorded in solvents of different solvent parameters of dielectric constant ε and refractive index η. Figs. 2 and 3 show the absorption and fluorescence spectra of 3C7H4M respectively in solvents with various polarity indices as shown in table 1.

Fig.2. Absorption spectra of 3C7H4M in various solvents

Fig3. Fluorescence spectra of 3C7H4M in various solvents.

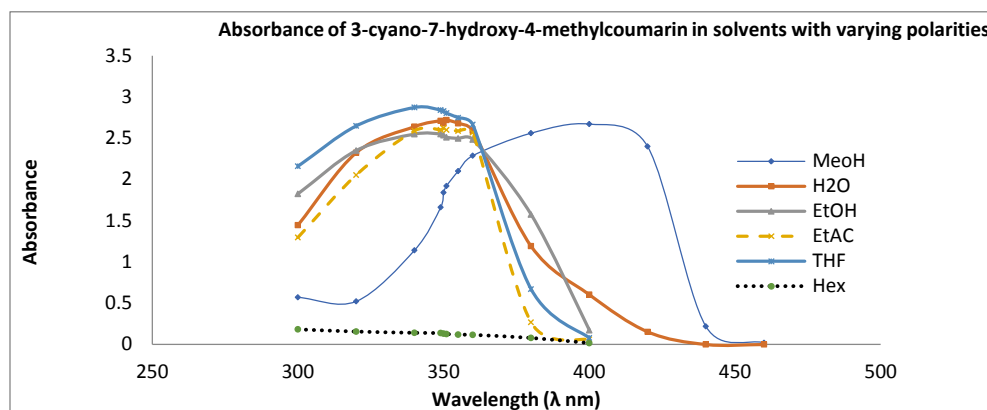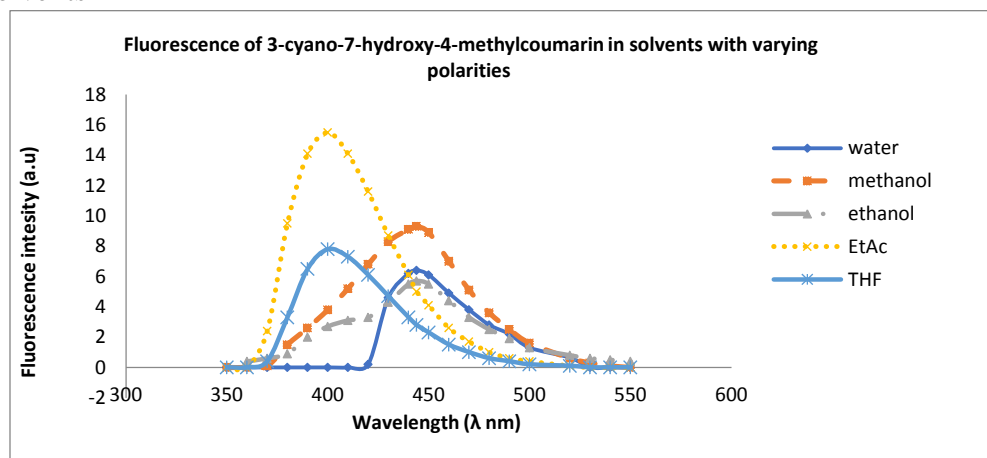The absorption and emission spectra of 3C7H4M show maximum values around 340nm and 400nm respectively for THF, 350nm and 400nm respectively for ethyl acetate, 349nm and 444nm for ethanol respectively, 349nm and 440nm for methanol and 400nm and 444 for water.

However, the hexane solution did not show any absorbance and emission. This resulted in stokes shift ranging from 04–60nm on changing the solvent from water to THF and the emission spectra. The absorption and emission maxima, dielectric constant and refractive index of 3C7H4M in different solvents are given in Table 1.

Table 1.Solvent effects on the positions of absorption and fluorescence maxima

Solvent	Polarity index	λ_{max} (Abs)	λ_{max} (Fluo)	$(v_f - v_a)$	ε	η
THF	4.0	340nm	400nm	60nm	7.6	1.4120
Ethyl Ac	4.4	349nm	400nm	50nm	6	1.3681
Ethanol	5.2	400nm	444nm	44nm	24.3	1.3428
Methanol	6.6	408nm	440nm	32nm	32.7	1.3335
Water	10.2	440nm	444nm	4nm	78.4	1.3303

Table 1 cont.

	$\tilde{V}a-\tilde{V}f$ (cm^{-1})	$\tilde{V}a+\tilde{V}f$(cm^{-1})	$f(\varepsilon, \eta)$	$g(\eta)$	$f(\varepsilon, \eta)+2g(\eta)$
THF	-	-	0.4379	0.2793	0.9966
Ethyl Acetate	54411.76	4411.76	0.3866	0.2424	0.8715
Ethanol	25387.85	6131.18	0.6398	0.2219	1.0837
Methanol	51298.7	5844.16	0.6660	0.2145	1.0952
Water	47522.52	2477.48	0.7121	0.2120	1.1362

The charge transfer band shows a shift of about 08–100 nm in the absorption spectra on changing the solvent from THF to water and the emission spectra show smaller shift as compared with the absorption   spectra.   The highly pronounced absorption shift between water and other solvents implies that the ground state energy distribution is affected to a greater extent possibly due to the polar nature of 3C7H4M.

The magnitude of Stokes shift varies between from 04–160nm. The values of the Stokes shifts are also indicative of the charge transfer transition. On changing the solvent from a low polar, like THF to high polar like ethyl acetate shows a difference in Stokes shift of about 9nm again indicative of a charge transfer transition. The large magnitude of the Stokes shift indicates that the excited state geometry could be different from that of the ground state. The general observation is that there is an increase in the Stokes shift values with increasing solvent polarity which shows that there is an increase in the dipole moment on excitation.

Figs. 4 and 5 show the spectral shifts (in cm^{-1}) $\tilde{v}_a - \tilde{v}_f$ and $\tilde{v}_a + \tilde{v}_f$ of 3C7H4M in polarity functions $f(\varepsilon, n)$ and$f(\varepsilon, n) + 2g(n)$. A linear progression was done data was fit to a straight line. The slopes m_1 and m_2 of the fitted lines shown in Figs. 4and 5.
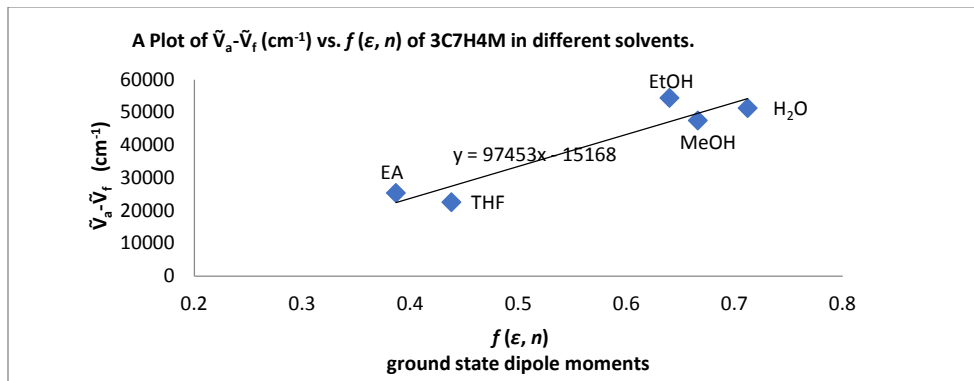
Fig.4. A Plot of $\tilde{V}_a$-$\tilde{V}_f$ (cm^{-1}) vs. $f(\varepsilon, n)$ of 3C7H4M in different solvents.
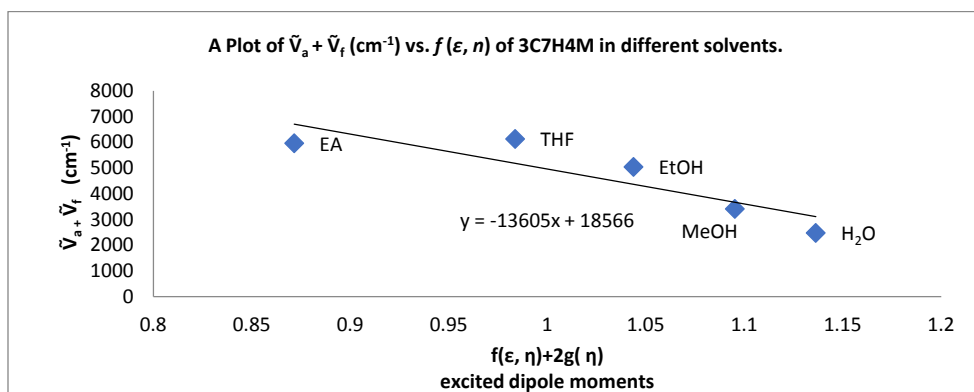

Fig.5. A Plot of $\tilde{V}_a$+$\tilde{V}_f$ (cm^{-1}) vs. $f(\varepsilon, n)$ of 3C7H4M in different solvents.

The slopes of Figs. 4 and 5 were found to be $m_1 = 97453$ cm^{-1} and $m_2 = 13605$ cm^{-1} and the Onsager radius (a) of solute was calculated using the equation;

$$a = \sqrt[3]{\frac{3M}{4\pi\rho N}} \simeq 3.8A$$

Where M is the molecular weight of the dye; ρ is the density of the dye; N is the Avogadro's number. We have approximated the density of this compound to be 1 g/mL. By using Eqs. (3) and (4), we get $\mu g = 5.349$ D and $\mu e = 7.954$ D and the change in the dipole moments ($\Delta\mu = \mu_g - \mu_e$) is 2.605 D. From Eqs. (3) and (4), the dipole moments μ_g and μ_e depends not only on m_1 and m_2 but also on radius of the solute. The linear dependence of spectral shifts on polarity function (Fig. 4 and 5) exhibits a good correlation. These experimental values were obtained in solution phase, where the solvent (matrix) is expected to introduce strong perturbation. Further it is evident from these results that, the changes in the dipole moments on electronic excitation are small.

Fig. 4 and 5 show images of epifluorescent microscopy of a plant cell stained by 3C7H4M in various polar solvents compared with Iodine. 3C7H4M stain in methanol almost compares with

the standard stain iodine. However, 3C7H4M in methanol appears to give brighter and clearer image of the cell. This is attributed to a higher fluorescence intensity of 3C7H4M in methanol unlike water and ammoniated water solutions.

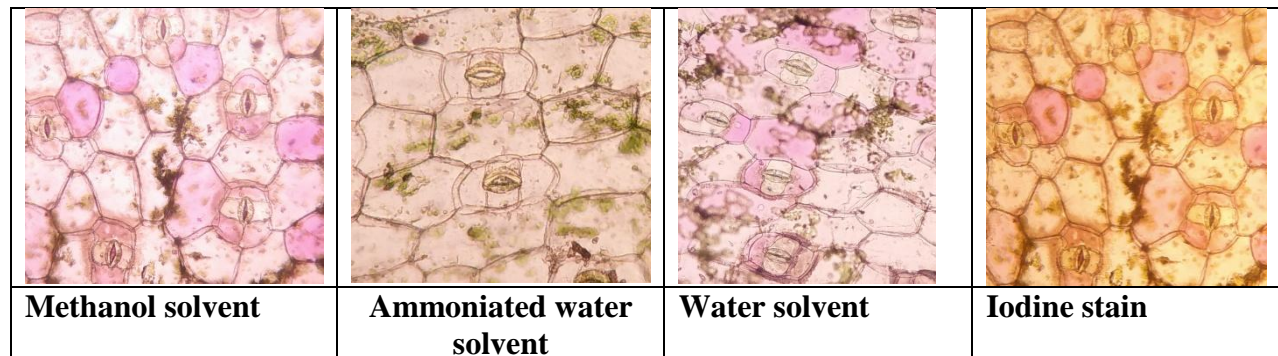| Methanol solvent	Ammoniated water solvent	Water solvent	Iodine stain

Fig.6. Images of living plant cells stained with 3C7H4M in various polar solvents compared with standard laboratory stain-Iodine viewed under a light microscope with resolution set at x10.

Conclusion

Both excitation and emission wavelengths of 3C7H4M in different solvents varying in polarity index has been determined. The Onsager radius has been calculated and the surface area of the molecule has been established, assuming the molecule as spherical and density is 1 g/mL. The determinations of dipole moments of C7H4M in the ground and excited states have shown that C7H4M is more polar in the excited state than the ground state. The results (fig.6) reveal that methanol is a better solvent for 3C7H4M in epifluorescence microscopy due to its polarity.

Conflict of interest statement

The authors declare that the research was conducted in the absence of any commercial or financial relationships that could be construed as a potential conflict of interest.

Acknowledgements

References

Biradar, D. S., Siddlingeshwar, B., & Hanagodimath, S. M. (2008). Estimation of ground and excited state dipole moments of some laser dyes. *Journal of Molecular Structure*, *875*(1–3), 108–112. https://doi.org/10.1016/j.molstruc.2007.04.005

Grotkopp, O., Mayer, B., & Müller, T. J. J. (2018). Diversity-Oriented Synthesis and Optical Properties of Bichromophoric Pyrrole-Fluorophore Conjugates. *Frontiers in Chemistry*, *6*, 579. https://doi.org/10.3389/fchem.2018.00579

Kadolkar, P. S., Patil, S. A., Kariduraganavar, M. Y., & Inamdar, S. R. (2019). *Evaluation of ground and excited state dipole moments of alexa fluor 350-NHS ester in binary mixtures of DMSO-water*. 030029. https://doi.org/10.1063/1.5100456

Kirsch, G., Abdelwahab, A., & Chaimbault, P. (2016). Natural and Synthetic Coumarins with Effects on Inflammation. *Molecules*, *21*(10), 1322. https://doi.org/10.3390/molecules21101322

Nagaraja, D., Patil, N. R., Kusanur, R. A., Patil, H. D., & Melavanki, R. M. (2012). *Estimation of Ground and Excited State Dipole Moments of Coumarin Derivatives by Solvatochromic Method*. *2*(12), 9.

Patil, N. R., Melavanki, R. M., Kapatkar, S. B., Ayachit, N. H., & Saravanan, J. (2011). Solvent Effect on Absorption and Fluorescence Spectra of Three Biologically Active Carboxamides (C1, C2 and C3). Estimation of Ground and Excited State Dipole Moment from Solvatochromic Method Using Solvent Polarity Parameters. *Journal of Fluorescence*, *21*(3), 1213–1222. https://doi.org/10.1007/s10895-010-0800-4

Perez-Rodriguez, E., Aguilera, J., & Figueroa, F. L. (2003). Tissular localization of coumarins in the green alga Dasycladus vermicularis (Scopoli) Krasser: A photoprotective role? *Journal of Experimental Botany*, *54*(384), 1093–1100. https://doi.org/10.1093/jxb/erg111

Raikar, U. S., Renuka, C. G., Nadaf, Y. F., Mulimani, B. G., Karguppikar, A. M., & Soudagar, M. K. (2006). Solvent effects on the absorption and fluorescence spectra of coumarins 6 and 7 molecules: Determination of ground and excited state dipole moment. *Spectrochimica Acta Part A: Molecular and Biomolecular Spectroscopy*, *65*(3–4), 673–677. https://doi.org/10.1016/j.saa.2005.12.028

Sharma, N., Jain, S. K., & Rastogi, R. C. (2007). Solvatochromic study of excited state dipole moments of some biologically active indoles and tryptamines. *Spectrochimica Acta Part A: Molecular and Biomolecular Spectroscopy*, *66*(1), 171–176. https://doi.org/10.1016/j.saa.2006.02.039

Taniguchi, M., & Lindsey, J. S. (2018). Database of Absorption and Fluorescence Spectra of >300 Common Compounds for use in PhotochemCAD. *Photochemistry and Photobiology*, *94*(2), 290–327. https://doi.org/10.1111/php.12860

Vequi-Suplicy, C. C., Coutinho, K., & Lamy, M. T. (2014). Electric dipole moments of the fluorescent probes Prodan and Laurdan: Experimental and theoretical evaluations. *Biophysical Reviews*, *6*(1), 63–74. https://doi.org/10.1007/s12551-013-0129-8

Zhang, X., Zhang, J.-J., & Xia, Y.-Y. (2008). Molecular design of coumarin dyes with high efficiency in dye-sensitized solar cells. *Journal of Photochemistry and Photobiology A: Chemistry*, *194*(2–3), 167–172. https://doi.org/10.1016/j.jphotochem.2007.08.004

Optical Characterization Of Co:Zno Films Fabricated By Anodization For Photocatalytic Water Purification

Judith Chebwogen[1], Christopher Maghanga[2], Mghendi Mwamburi[3], Munyati Onesmus[4], Sylvester Hatwaambo[5], Sellah Kebenei[6]

[1]Kabarak University, P.O. Box Private Bag, Kabarak, 20157, Kenya
Tel: +254 726 472 810, Email: judithkoskey86@gmail.com
[2]Kabarak University, P.O. Box Private Bag, Kabarak, 20157, Kenya
Tel: +254 722 986 967, Email: cmaghanga@kabarak .ac.ke
[3]University of Eldoret, P.O Box 1125, Eldoret, 30100, Kenya
Tel: +254 722 375 112, Email: mghendim@gmail.com
[4]University of Zambia, P.O. Box 32379, Lusaka, Zambia
Tel: +260 966754245, Email: omunyati@gmail.com
[5]University of Zambia, P.O. Box 32379, Lusaka, Zambia
Tel: +260 96 6754245, Email: shatwaambo@gmail.com
[6]Kabarak University, P.O. Box Private Bag, Kabarak, 20157, Kenya
Tel: +254 726 472 810, Email: judithkoskey86@gmail.com

Abstract*:* While the sixth sustainable development goal to be achieved by 2030 is clean water and sanitation, there is still a global challenge in the supply of adequate clean water due to population growth and urbanization. This necessitates coming up with more affordable approaches of managing waste water. Photocatalytic degradation of pollutants has proved to be one of the promising ways of purifying water. This study aimed at preparing Cobalt doped ZnOfilms to be used in photocatalytic water purification. ZnO films were fabricated by anodization and Cobalt incorporated. Heat treatment was done at 250^0C. Optical characterization was done using a UV-VIS NIR spectrophotometer to obtain reflectance data which aided in determining the optical properties of the films. Data analysis showed a decrease in ZnO reflectance and optical band gap on incorporation of Cobalt. This implied an increase in the absorption of the films which is a fundamental property in photocatalytic water purification. Hence Cobalt doped ZnOfilms have good photocatalytic properties and can be used for photocatalytic water purification.

1. Introduction

Photocatalysishas proved to be one of the most promising techniques for purification of waste water by the chemical utilization of solar energy where hazardous organic pollutants are degraded, Hoffman *et al*., (1995).ZnOwhich is a wide band gap semiconductor with a band gap of 3.31eV has been widely used in designing of diodes, biosensors, as antibacterial agents and photocatalysts because it is cheap, readily available and non-toxic. In photocatalysisit is used to speed up the degradation rate.Its wide band gap however limits its photocatalytic activity hence the need to improve its activity. Metal ions such as Mn^{2+},Cu^{2+},Ag^{2+} and Co^{2+}have been used to alter the optical and photocatalytic properties and Cobalt ions are preferred because their ionic radius(0.745Å)is similar to that of Zinc(0.74Å), Woo *et al*., (2014).ZnO:Co films can be fabricated using different techniques such as spray pyrolysis, sol-gel, sputtering and anodization, Kulkrani and Shirsa (2015).In this study, we seek to fabricate Co:ZnO films by anodizationand

characterize them optically consequently its application in photocatalytic water purification since optical properties determine the photocatalytic activity.

The problem

Water is vital for survival of all living things but its pollution is one of the major threats to life.Water pollution has resulted from rapid population growth and urbanization and this threatensthe fundamental human rights, such as the right to life, health, wellbeing, safe work, as well as protections of children and the most vulnerable. The organic pollutants in water are hazardous and cause diseases or death. Because of this global and national threat there is need for cost effective water treatment techniques such as photocatalysis. Although ZnO has been applied in photocatalysis, its band gap is wide resulting in a narrow range of the solar spectrum absorbed. This implies that there is need to narrowits band gap hence improving its photocatalytic activity.

1.1 Objectives

i) To fabricate ZnO thin films by anodization.
ii) To pigment the fabricated ZnO films with Cobalt.
iii) To determine the optical properties of pure and Cobalt pigmented ZnO films by optical characterization.

2. Literature review

In a study of the photocatalytic activity of ZnO nanoparticles synthesized by combustion method done by Nagaraju*et al.,* (2017) who showed the band gap of *ZnO* as 3.29 eV. Photocatalytic results in this study showed ZnO as a promising photocatalytic material.Kuriakose*et al.,*(2014), studied enhanced photocatalytic activity of Co doped *ZnO*nanodisks and nanaorods prepared by wet chemical method and reported that doping *ZnO*nanodisks and nanorods with Co enhanced their photocatalytic activity.Poongodi*et al.,* (2015) stated that Cobalt doped *ZnO* was seen to be more photocatalytic than the pure *ZnO*. They attributed this to the increase in ZnO crystal size when doped with Cobalt.Borhani and Amrollahi (2017) observed a shift in the ZnO band edge towards longer wavelengths on doping with Cobalt. They also reported a decrease in the absorption coefficient with increasing wavelengthand an increase with the extinction coefficient with Cobalt doping.

3. Methodology

Zinc plates of desired size were mirror polished, sonicated in ethanol, rinsed and dried in air. Pure ZnO plates were prepared by anodization method. The schematic diagram for anodization method is shown in figure 1. A constant voltage of 10V was maintained for 60 minutes using 0.5M oxalic acid as the electrolyte, zinc as the working electrode and graphite the counter electrode.This was done at room temperature after which the anodized zinc sheets were rinsed in distilled water and dried in air. Cobalt was electrodeposited in some of the anodized ZnO for 20s and 60 seconds using a 20V ac power supply. Post anodization heat treatment done by heating the plates at 523K for 2 hours.
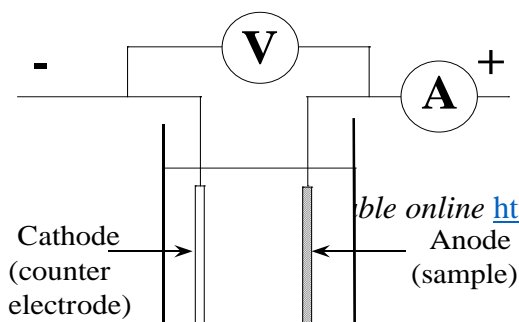
ble online http://ir.kabarak.ac.ke/handle/123456789/1

Cathode
(counter
electrode)

Anode
(sample)

Figure 1: Schematic diagram for anodizationmethod. Nemes*et al.,* (2011)

Optical characterization was done using a perkinelmerUV/VIS/NIR Lambda 19 spectrophotometer equipped with an integrating sphere to evaluate the optical properties of the pure and Cobalt pigmented ZnO films. Reflectance measurement was done in the solar range 300nm < λ < 2500nm. Further data analysis was done using the SCOUT software which aided in the determination of the optical properties of the fabricated films.

4. Results

4.1 Reflectance

Figure 2 shows the spectra for the measured reflectance for the polished Zinc metal before anodization and the as deposited ZnO and Co:ZnO films.
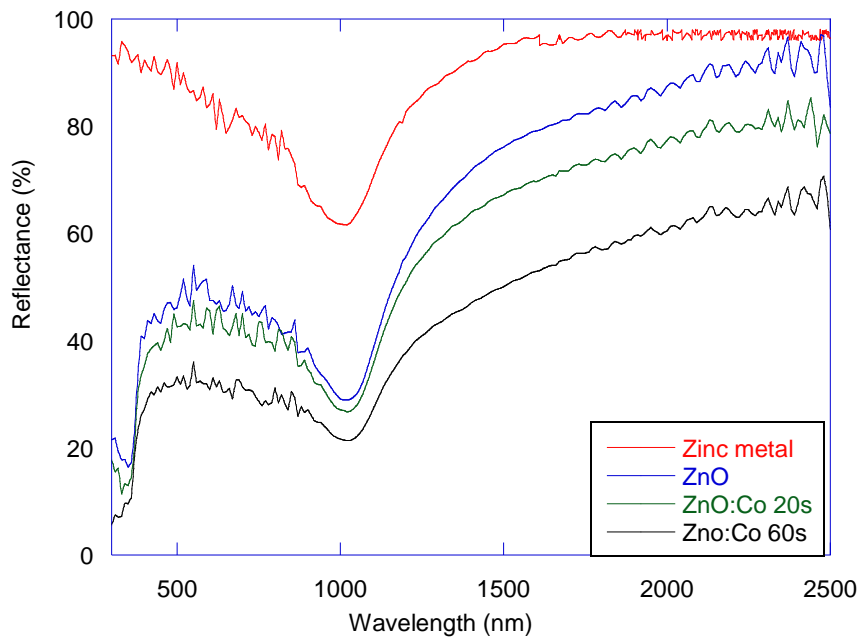
Figure 2: Measured reflectance spectra for polished zinc metal, pure ZnO and Co:ZnO

Polished zinc metal has a higher reflectance more than 60% because of its shiny nature. The reflectance for pure ZnOis higher thanfor Co:ZnO. This can be attributed to the darkening of the ZnO films when they are pigmented with Cobalt. A sharp decrease in the pure and Co:ZnOreflectance is observed at low wavelengths about 348nm. This decrease gives the absorption edge of the films which is agreement with the fact that ZnO absorbs in the UV region of the solar spectrum. The decrease in reflectance of the Cobalt pigmented ZnO films is indicative of an increase in the absorption.

4.2 Absorption coefficient

Figure 3 shows the absorption coefficient as a function of wavelength.
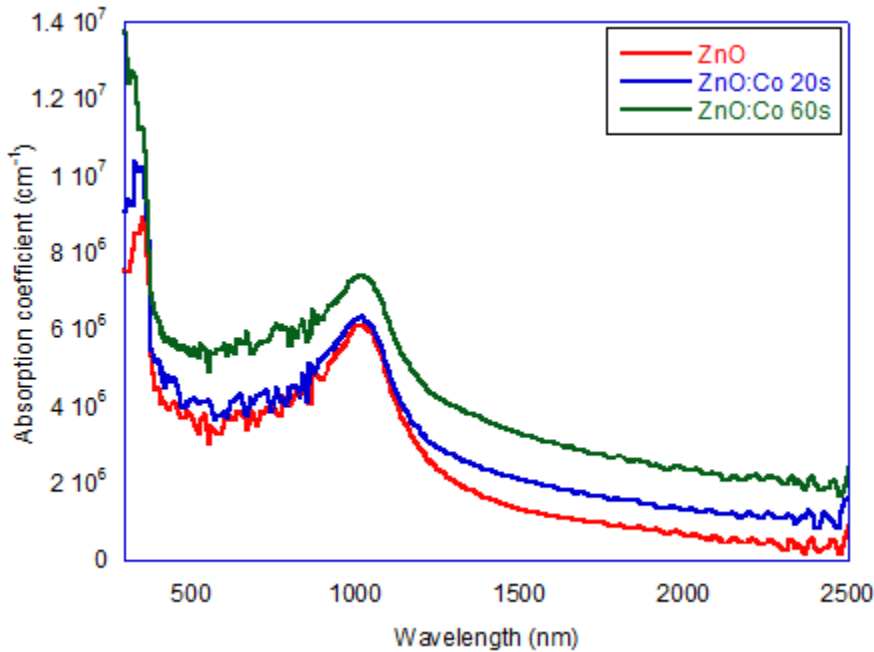
Figure 3: Absorption coefficient as a function of wavelength

The absorption coefficient for the pure and Cobalt pigmented ZnO films is observed to sharply increase at low wavelengths representing the UV region of the solar spectrum. This also further explains the high absorption of ZnO in the UV region due to its wide band gap. Cobalt pigmented ZnO has a higher absorption coefficient in the lower wavelengths than pure ZnO. This is attributed to the decrease in reflectance on pigmenting hence an increase in absorption. At higher wavelengths, the absorption coefficient remains low showing low absorption by the films.

4.3 Band gap

The optical band gap for ZnO which is a direct band gap semiconductor is as shown in figure 4.

Figure 4: Graph showing the optical band gap of the fabricated films

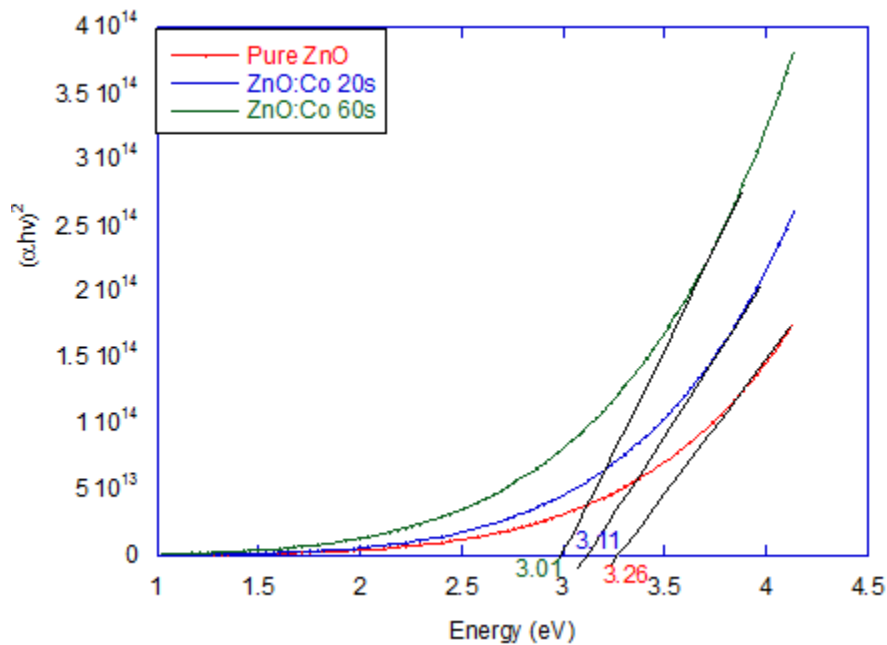The optical band gap of pure ZnO is 3.26e V. A decrease in the band gap is observed as the ZnO films are pigmented with Cobalt. The decrease in band gap is an indication of an increase in the absorption of the films as confirmed by the reflectance and absorption coefficient. This is attributed to the red shift in the absorption edge of the ZnO films which results from the Cobalt ions being incorporated into the ZnO crystal structure. This leads to the formation of impurity levels between the ZnO band gap hence narrowing it.

Recommendations

The results obtained and reported in this work show a clear influence of the Cobalt pigmenting on ZnO optical properties. This study was confined to a narrow study of the optical properties. Photocatalysis is also influenced by other factors like the structure and surface morphology. It is therefore recommended that structural characterization of the films be done to confirm the surface morphology and the crystal structure and orientation. This can be studied using Scanning Electron Microscopy (SEM), Transmission Electron Microscopy (TEM) and X-ray Diffraction (XRD).

Conclusion

Pure and Cobalt doped ZnO films were successfully fabricated by anodization.Cobalt pigmenting decreases the reflectance of ZnO films hence an increase in absorption while absorption coefficient increases with Cobalt pigmenting and decreases at higher wavelengths.Band gapZnO is narrowed by pigmenting it with Cobalt. The more the Cobalt deposited in ZnO films the more the decrease in band gap.The optical properties of the Cobalt doped ZnO show that ZnOphotocatalysis can be enhanced by pigmenting it with Cobalt.

Acknowledgement

References

BorhaniZarandi, M., &AmrollahiBioki, H. (2017). Effects of Cobalt Doping on Optical Properties of ZnO Thin Films Deposited by Sol–Gel Spin Coating Technique. *Journal of Optoelectronical Nanostructures*, *2*(4), 33-44.

Hoffmann, M. R., Martin, S. T., Choi, W., &Bahnemann, D. W. (1995). Environmental applications of semiconductor photocatalysis. *Chemical reviews*, *95*(1), 69-96.

Kulkarni, S. S., &Shirsa, M. D. (2015). Optical and structural properties of zinc oxide nanoparticles. *IJARPS*, *2*, 14-18.

Kuriakose, S., Satpati, B., &Mohapatra, S. (2014). Enhanced photocatalytic activity of Co doped ZnOnanodisks and nanorods prepared by a facile wet chemical method. *Physical Chemistry Chemical Physics*, *16*(25), 12741-12749.

Nagaraju, G., Shivaraju, G. C., Banuprakash, G., &Rangappa, D. (2017). Photocatalytic activity of ZnO nanoparticles: synthesis via solution combustion method. *Materials Today: Proceedings*, *4*(11), 11700-11705.

Nemes, D., Moldovan, V., Bruj, E., Jumate, N., & Vida-Simiti, I. (2011). Porous anodic alumina films obtained by two step anodization. *Bulletin of the Transilvania University of Brasov. Engineering Sciences. Series I*, *4*(2), 75.

Poongodi, G., Anandan, P., Kumar, R. M., &Jayavel, R. (2015). Studies on visible light photocatalytic and antibacterial activities of nanostructured cobalt doped ZnO thin films prepared by sol–gel spin coating method. *SpectrochimicaActa Part A: Molecular and Biomolecular Spectroscopy*, *148*, 237-243

Woo, H. S., Kwak, C. H., Chung, J. H., & Lee, J. H. (2014). Co-doped branched ZnO nanowires for ultraselective and sensitive detection of xylene. *ACS applied materials & interfaces*, *6*(24), 22553-22560.

Structural Properties of Photocatalytic Copper Pigmented Anodized titanium

Peter c. Owino[1*], Maurice M. Mwamburi[1], David Waswa[1], Margaret E. Samiji[2], Nuru R. Mlyuka[2], GraceA.Kinunda[2], Christopher Maghanga[3].

[1]Department of Physics, University of Eldoret,
P. O. Box 1125 – 30100, Eldoret, Kenya
[2]Department of Physics, Department of Chemistry,University of Dar es Salaam,
P. O. Box 35063, Dar es Salaam, Tanzania
[3]Kabarak University, P.O. Box Private Bag, Kabarak, 20157, Kenya
Tel: +254 722 986 967, Email: cmaghanga@kabarak .ac.ke

[*]Corresponding author e-mail: owinop3@gmail.com

Abstract

The performance of TiO_2photocatalyst depends on its surface morphology andthe orientation of its crystal structure. In this study, commercial pure grade 1 titanium substrate was anodized at 200V for different anodization times, pigmented and annealed for a period of 450^0C for 4 hours. Structural properties of the samples was done using AFM, XRD and SEM. Prolonging anodization time engineered the formation of pores and eventual pore merging on the surface of the TiO_2 film thereby significantly influencing the surface morphology and crystallinity of the sample.The XRD measurements confirmed the coexistence of both rutile and anatase phases inthe samples.

Keywords: TiO_2, Photocatalyst, anodization, pigmentation, stuctual properties.

Introduction

TiO2photocatalysts has been widely studied due to its chemical stability, optical properties, biological and environmentally benefits. The photocatalytic performance of TiO2 materials are determined by the morphology and phase composition of the material.TiO2 materials exist in three phases namely anatase, rutile and brookite. In their single phase structures, anatase has been reported to have the highest photocatalytic efficiency compared to the other two phases(Hanaor et al, 2011). Anataseis mostly the first phase formed during titanium treatment due to its constrained structural re-arrangement which forms this phase from an amorphous precursor and a lower surface energy comparedto the rutile phase (Shin et al, 2005; Zhang and Banfield, 1998). Rutile is deemed to be thermodynamically stable form of the crystal structure at all temperatures, phase transformation fromanatase to rutile generally occurs when TiO2 materials are heated in air in the absence of impurities or dopants at a temperature of 650°C and above. Dopants such as Cu, Pt and Cr influence the phase transformation from anatase to rutile by changingthe oxygen vacancy energy levels and enhancing the structural re-arrangement involved in the transformation (Arroyo et al, 2002). Less research has been carried out on brookitephase due to its reduced photocatalytic activity (Di Paola et al, 2013; Srivatsa et al, 2008). Studies have shown that a mixtue of anatase-rutile phase with certain composition ratio exhibits superior photocatalytic performance due to its improved separation of charge carrier

through the trapping of conduction band electrons in the rutile phase (Collins-Martinez et al, 2007; Ohno et al, 2003).

When TiO_2 photocatalyst is illuminated with light of energy higher than the band-gap, an inter-band transition is induced and electron-hole pairs generated. Some of these photogenerated pairs achieve charge separation and diffuse to the TiO_2 surface, react with air or water and eventually generate OH radicals and O⁻ superanions, which attack the organic compounds adsorbed on the TiO_2 surface, removing them by transforming into CO_2 and H_2O. Thus the surface of TiO_2 photocatalyst converts into a strong oxidizer which attack and clean the water and air by photodestruction of adsorbed contaminants.

Materials and Methods

The pre-treatment processes vary from rinsing, degreasing and etching. Grade 1 titanium foil of 0.3mm thickness was cut in rectangular pieces of 60mm×30mm specimens, the sample was degreased in acetone solution for five minutes at ambient temperature after which etching (Acid activation) followed up. Acid activation was performed in a mixture of nitric acid, hydrofluoric acid and water for 5 seconds to remove the natural titanium oxide layer and surface contaminants after which it was rinsed with distilled water.

Anodization was therefore done in an electrolyte consisting of 0.75M H_2SO_4, 0.075% wt HF and distilled water which was kept in a bath at a temperature of 25˚C, magnetic stirring was done at about 800 rpm throughout the anodizing period. Inter electrode distance of 1cm was maintained with the anode to cathode area ratio of 1:4, with aluminium as the counter electrode. Anodization was done at a constant voltage (potentiostatic) of 200Volts from 20seconds to 30minutes after which the samples were rinsed in de-ionised water thoroughly before drying in air and storing for pigmentation.

The electro deposition cell was prepared with 0.1M $CuSO_4$:$5H_2O$ electrolyte, pigmentation of the anodized plate was done at 12volts for a period of 5 seconds. The anode was made of copper plate fixed at a distance of 1cm from the titanium cathode plate. Annealing of Titanium plates

Annealing was done by Muffle furnace for a period of four hours at 450˚C$\pm$ 5^0C. The samples were placed inside Petri dishes, placed in the furnace and the door locked tightly to avoid any contact with the outside environment.

Results and Discussion

Atomic Force Microscopy

The AFM images revealed distinct topography for all samples. The morphology and distribution of the pores were found to be affected by the duration of anodization. The AFM images of the un-anodized Ti sample and those anodized at different time intervals of 1 minute, 2 minutes, 3 minutes, 10 minutes and 30 minutes are as shown in figure 1.
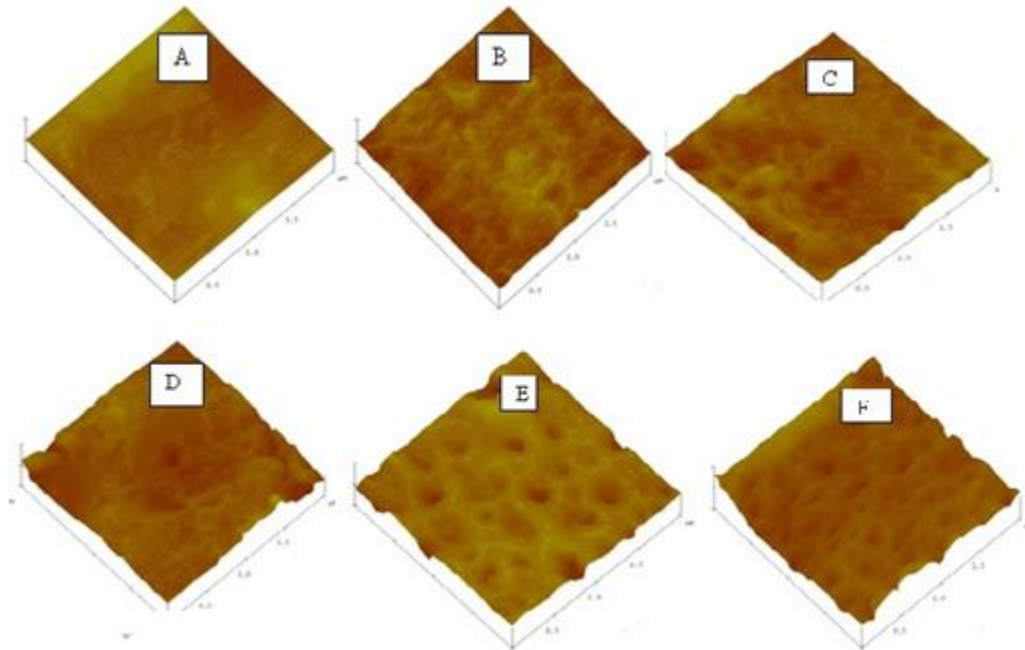
Figure 1: Effect of anodization time on the morphology of the samples, (A) un-anodized Ti (B) 1 minute (C) 2 minutes (D) 3 minutes (E) 10 minutes and (F) 30 minutes.

Before anodization, the surface of metallic titanium sample was smooth and homogeneous as seen in figure 1 A. Figure 1 B, C and D shows that in the initial stages of anodization, there is uneven distribution of the oxide layer on the Ti samples with a low surface roughness. For longer anodizationtime, the formation of pores becomes more pronounced and unevenly distributed. Each sample scanned at different positions exhibited the same topography but with a slight shift in the surface features. The Ti sample anodized for 30 minutes exhibited unique features as shown in figure 2. The image shows an inhomogeneous distribution of surface features with a continuous oxidation of the surface on some parts of the sample but not on other parts. This finding can be explained based on the three processes namely, field-enhanced oxidation of titanium foil, field–assisted oxide dissolution, andchemical oxide dissolution (Quan*et al*, 2005).

During field–enhanced oxidation, titanium metal undergoes a process of oxidation leading to the growth of an oxide layer on the metals' surface, as the oxygen ions in the electrolyte solution move towards the interface of the metaland the oxide layer. During field-assisted oxide dissolution, the oxide layer dissolves into the electrolyte due to the movement of titanium ions from the metal-oxideinterface through the oxide layer into the solution. The presence of hydrofluoric acid (HF) in the electrolyte helps in accelerating the rate ofdissolution of the oxide layer by consuming titanium ions in solution (Gong*et al*, 2001). Since this process has norestriction to the occurrence of pores and pore widening, the extensive dissolution of the oxide layer taking place when the anodization period is prolonged results to pore merging and the eventual loss of the pore structures as seen in figure 2.
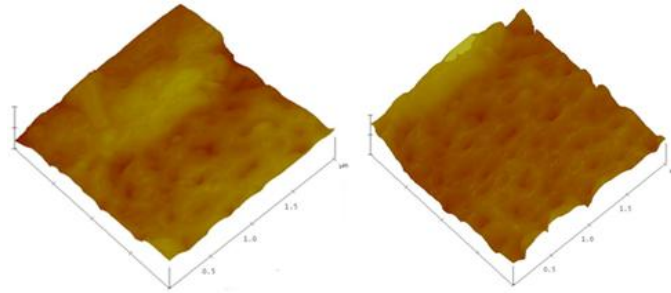
Figure 2: Surface morphology of sample taken at different positions and anodized for 30 minutes.

Surface roughness

Surface roughness is an important characteristic of the oxide film and significantly affects its properties. In order to investigate the effect of anodization on the surface roughness of the oxide film, the average surface roughness (*Ra*) and root mean square of the sample roughness (*Rms*) were obtained by allowing the software to scan through different sections of two-dimensional AFM samples' morphology. It can be seen from figure 3 that the *Ra* and *Rms* of the oxide film on the surface of the sample anodized for 1 minute, 2 minutes, 3 minutes, 10 minutes and 30 minutes are 18.87 and 24.63, 21.46 and 33.04, 39.17 and 51.27, 40.95 and 55.71, 77.08 and 90.81, respectively, which indicates that the roughness of the oxide film increased with the increase of anodization time.
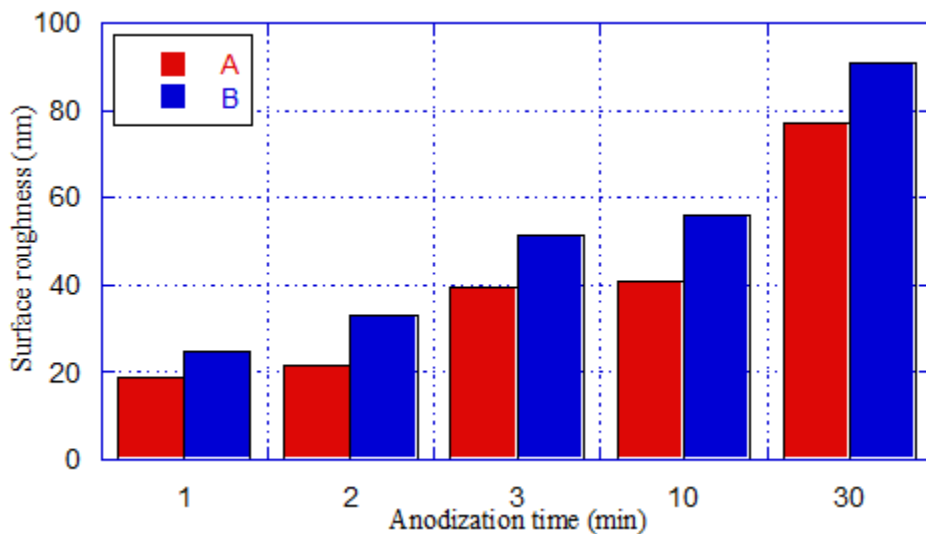

Figure 3: Comparison of sample's surface roughness against anodizing time A) the average surface roughness (*Ra*) and B) root mean square of the sample roughness (*Rms*)

Scanning Electron Microscopy

Figure 4 shows SEM images for samples anodized at 200 V, pigmented and annealed at 450^0C for 4 hours at different time intervals of 1 minute, 2 minutes, 3 minutes, 10 minutes and 30 minutes. It is clear that thestructure and morphology of the oxide layers on Ti samples change when the duration of anodization is prolonged.
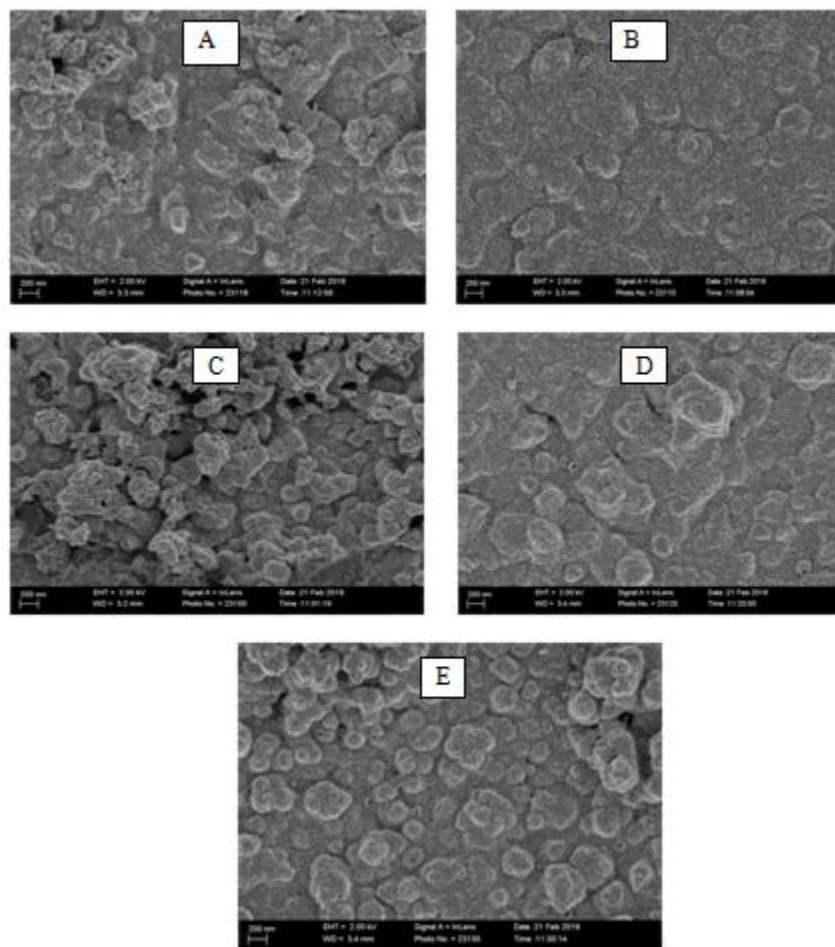

Figure 4: SEM images for samples anodized at 200 V, pigmented and annealed for 450^oC for 4 hours. (A) anodized for 1 min, (B) 2 min, (C) 3 min, (D) 10 min and (E) 30 min.

The sample shown in Figure 4(A) exhibited hilly like features which represents the formation of the metal oxide layer with porous structure, implying that Ti starts to be oxidized to Ti^{4+} ions at the surface layer of the Ti metal sample at this stage. Figure 4(B) shows an almost compact and smooth surface morphology after anodizationperiod of 2 minutes. It is interesting to note that by prolonging the anodizing time to 3 minutes, a layer of flowershaped features with irregular grains forms and covers the top layer of the TiO_2sample as seen in Figure 4 (C). Figure 4 (D) showed irregular grains with tiny cracks as samples are anodized for 10 minutes. In Figure 4 (E), the surface structure appears to be compact with formation of hill like structures in some sections of the sample. The whole process of grain and pore formation is due to the Electric field dissolution which is induced under applied potential, which eventually produces pores and grain

like structures. It is noteworthy that field-assisted oxidation and dissolution involves the formation of an oxide layer and the dissolution of that oxide.

X-ray diffraction measurement

Figure 5 shows a typical XRD pattern of TiO_2 film anodized at different time intervals, pigmented and annealed for duration of 450 ^{0}C for four hours.The samples had diffraction peaks at 2θ values of 27.9°, 37.0°, 61.81^0 and 69.5^0, that can be readily attributed to (110), (101), (002) and (112) planes which correspond to a tetragonal crystal structure of rutile phase,while the peak at 38.8°, 51.75^0 and 75.1^0 can be attributed to the (004), (105) and (215) plane of anatase TiO_2.This confirms the coexistence of both rutile TiO_2 and anatase TiO_2 phases in the annealed samples. The diffraction peak at 61.81^0 identified the presence of CuO coordinated to the metal cation Ti^{4+}.

The intensity of the (101) peak is the strongest in all peaks corresponding to rutile phase which indicates that the growth of TiO_2 is highly oriented along the (101) plane. Diffraction peaks (110) and (004) grew in intensity compared to the unanodized TiO_2 sample with peak (110) being more intense at anodization time of 1 min.
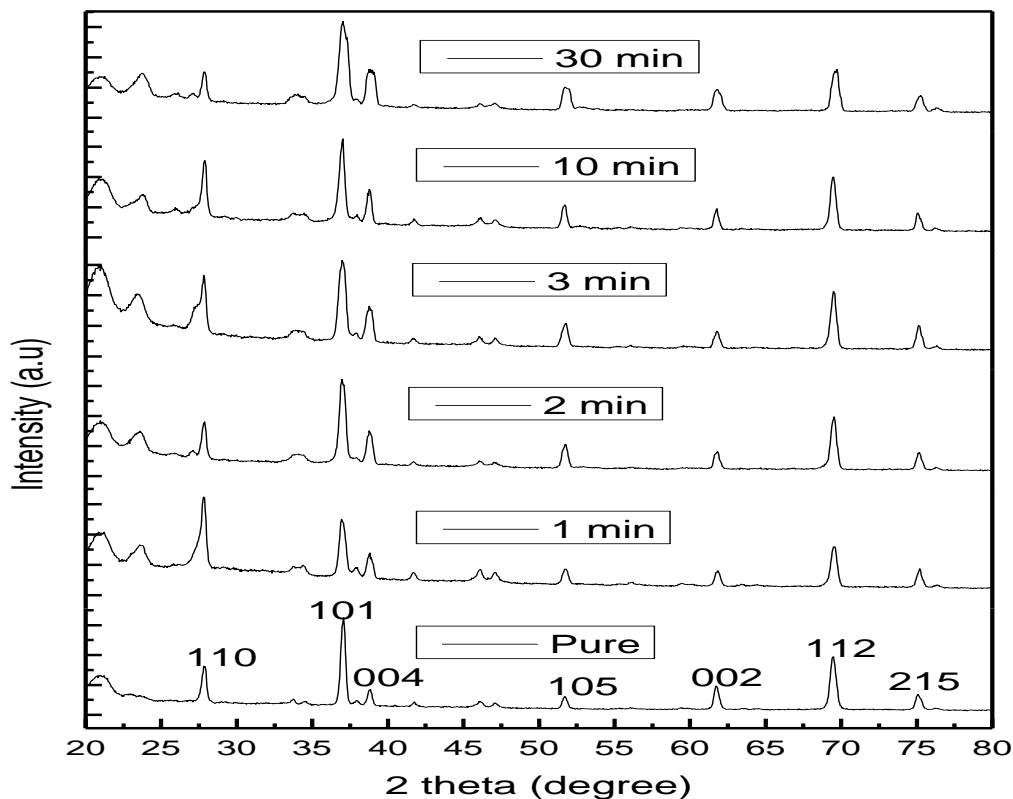
Figure 5: XRD patterns of TiO_2 anodized at 200 V, pigmented and annealed at 450 °C for 4 hours with anodizing time of 0min for pure sample, 1 minute, 2 minutes, 3 minutes, 10 minutes and 30 minutes.

Themean crystallite size of TiO_2 films was calculated usingthe Scherrer's formula

$$D = \frac{K\lambda}{\beta \cos\theta}$$ 1

Where, D is the average crystallite size, λ is the X-ray wavelength, β is the full width at half maximum (FWHM) of the dominant peak and θ is the Bragg angle.The pure unanodized TiO_2 film exhibited a crystallite sizeof 0.37 nm which was higher than the anodized ones. At 1 minute, 2 minutes, 3 minutes, 10 minutes and 30 minutes there crystallite size was 0.19 nm, 0.22 nm, 0.25 nm, 0.26 nm and 0.18 nm. This trend shows an increase in the crystallite size from 1 minute of anodization then an abrupt decrease towards anodization time of 30 minutes.

The dislocation density was calculated using the relations

$$\delta = \frac{1}{D^2}$$ 2

From the calculation, the dislocation density decrease with increase in anodization time which implies a decrease in lattice imperfection due to the increase in crystallite size. At anodization time of 30 minutes, the dislocation density increases.

The micro strain was calculated using the relations

$$\varepsilon = \frac{\beta \cos\theta}{4}$$ 3

The strain gets lower for increasing anodization time but increases at 30 minutes.

Table 1 shows the effect of anodization time on the average crystallite size (D), dislocation density (δ) and micro strain (ε) of the samples

Anodization Time	Average Crystallite size (D)	Dislocation Density (δ)	Micro Strain (ε)
1 minute	0.19	27.7	0.186
2 minutes	0.22	20.7	0.166
3 minutes	0.25	16.0	0.142
10 minutes	0.26	14.8	0.139
30 minutes	0.18	30.9	0.199

Conclusion

Prolonging the anodization time engineers the formation of pores, pores merging and eventual loss of pore structure of the TiO_2 film thereby significantly influencing the surface morphology and crystallinity of the sample.

The XRD measurements confirmed the coexistence of both rutile and anatase phases inTiO_2 samples anodized at 200V, pigmented and annealed at a temperature of 450^0C for 4 hours.

Acknowledgement

References

Arroyo R, Cordoba G, Padilla J and Lara V. (2002), Materials Letters, 54, 397-402.

Collins-Martinez V, Ortiz A and Elguezabal A. (2007), Influence of the anatase/rutile ratio on the TiO2 photocatalytic activity for the photodegradation of light hydrocarbons. International Journal of Chemical Reactor Engineering. 5.

Di Paola A, Bellardita M and Palmisano L. (2013), Brookite, the least known TiO_2photocatalyst. Catalysts. 3(1): p. 36-73.

Gong D, Grimes C, Varghese O, Hu W, Sing R, Chen Z and Dickey E. (2001). Titanium oxide nanotube arrays prepared by anodic oxidation, J.Mater.Res.,16, 3331.

Quan X, Yang S, Ruan X, and Zhao H. (2005). Preparation of titania nanotubes and theirenvironmental applications as electrode, Environ.Sci.Technol. 39, 3770-3775.

Srivatsa K., Bera M and Basu A. (2008), Pure brookitetitania crystals with large surfacearea deposited by plasma enhanced chemical vapour deposition technique. Thin SolidFilms. 516(21). 7443-7446.

Hanaor D, Triani G, Sorrell C. (2011), Surface and Coatings Technology 205(12), 3659-3664.

Ohno T, Tokieda K, Higashida S and Matsumura M. (2003), Applied Catalysis A,244, 383-391.

Shin H, Jung H, Hong K and Lee J. (2005), Journal of Solid State Chemistry, 178,15-21.

Zhang H, and Banfield J. (1998), Journal of Materials Chemistry, 8, 2073-2076.

Equation of State for a 2D System

Gloria I. Murila, [1] George S. Manyali, [1] James Sifuna, [1,2,3]

[1]Computational and Theoretical physics group (CTheP), Department of Physics, Masinde Muliro University of Science and Technology, 190-50100, Kakamega, Kenya

[2]Materials Modeling Group, Department of Physics and Space Sciences, The Technical University of Kenya, 52428-00200, Nairobi, Kenya

[3]Department of Natural Sciences, The Catholic university of Eastern Africa, 62157 -00200, Nairobi, Kenya

Abstract

We have described a simple theoretical model of an equation of state (EOS) for a two-dimensional system. The goal was to give a clear description of the interplay between hydrostatic change in surface area and the two dimensional in-plane pressure (F). Of interest from this described EOS, was the measure a material's resilience to isotropic stretching (γ) that can in principle be viewed as the layer modulus. To this date, few attempts have been made to obtain accurately the layer modulus of 2D systems. We studied using density functional theory as implemented in the Quantum ESPRESSO computer code, a number of monolayer systems; graphene, Boronitrene, dichalcogenides and Janus chalcogenides. The results found out in this study showed that of the above honeycomb structures, graphene was the most resilient to stretching with a value of C = 206.6 N/m followed by boronitrene BN = 177.3 N/m. The layer modulus of the dichalcogenides and Janus chalcogenides was seen to be competing but not as large as that of graphene or boronitrene. Apart from the layer modulus, we were also able to use the EOS to predict isotropic intrinsic strength of the listed systems. It was observed that the intrinsic stress was proportional to the layer modulus. This project does not just satisfy our knowledge thirst but can also be used by experimental groups in fabricating hard 2D materials.

Key words: EOS, First-principles, Density functional theory, Layer modulus.

1. Introduction

1.1 Two-dimensional materials

A part from electrical and optical properties of materials, mechanical properties feature as important aspects in exploring a new material (Liu & Wu, 2015). Mechanical properties provide a key criteria for discovering, selecting and refining new super hard materials that have wider applications in people's life.

The recent discovery of a two-dimensional (2D) graphene (Novoselov, *et al.,* 2004) & (Liu & Wu, 2015) (Geim, 2009), has opened-up doors for exploring materials whose fundamental properties are depended on its dimensionality. Among explored materials are the transition-metal dichalcogenides (TMDs), which consist of one transition-metal layer such as Hf, Ti, Zr, Mo,W, V, Nb, and Ta sandwiched between two chalcogen layers (S, Se and Te) to form a unit cell, in which metalchalcogens are covalently bonded within the plane (Chhowalla, *et al*., 2013). These

2D TMDs can form both out-of-plane and in-plane heterojunctions (Yifei, et al., 2015), (Duan, et al., 2014) & (Li, et al., 2015).

As far as we know, a mixed monolayer of MoSSe does not exist in nature, but its structure was theoretically predicted for the first time in 2013 (Cheng, Zhu, Tahir, & Schwingenshlogl, 2013), and after a short time it was successfully synthesized using the modified chemical vapour deposition (CVD) method (Lu A. , et al., 2017). To fabricate it, Lu and co-workers synthesized a monolayer of MoS_2 using CVD on SiO_2 substrate, then separated the top-layer S atoms and replaced them with H atoms using hydrogen inductively coupled plasma, and, finally, replaced H atoms with Se atoms using thermal salinization. S atoms in MoS_2 were completely replaced by Se atoms with the formation of a mixed MoSSe monolayer. Later, Kandemir and Sahin (Kandemir & Sahin, 2018) studied the structural, vibrational and electronic properties of the stable WSSe single layer. In addition, they studied bilayer stacking order in the hypothetical WSSe 2H-structure. Most recent studies have shown that by breaking the out-of-plane structural symmetry, a new kind of heterojunction is formed leading to a structurally stable Janus SMoSe monolayer (Lu, et al., 2017). This particular TMD consists of three layers of atoms formed by sulphur, molybdenum, and selenium. Great efforts have been devoted into the studies of various properties of single layer MoSSe (Ma, et.al, 2018) for insistence its hardness

In this study we have described the reaction of Janus to conditions of applied 2D pressure called the force per unit length $\mathcal{F}$ and we have shown how to obtain a layer modulus which is synonymous to the 3D bulk modulus.

1.2 Theoretical frame work

In a 2D set up an in-plane hydrostatic force will by default course a uniform change in its area. This force may be expressed as a derivative of energy with respect to the 2D surface area as

$$\mathcal{F} = -\frac{\partial E}{\partial A} \qquad\qquad 1$$

Where E, is the energy and A, is the area of the 2D system. From eqn. 1, can be denotes that if $\mathcal{F}$, is positive then we will have a compression while negative $\mathcal{F}$, denotes a uniform stretching. Proceeding we well represent the layer modulus of a 2D as

$$\gamma = -A\frac{\partial \mathcal{F}}{\partial A} \qquad\qquad 2$$

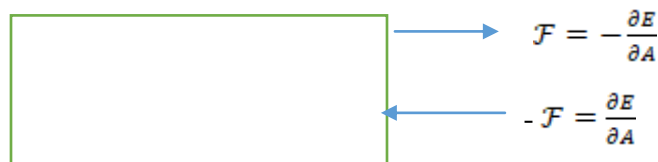The negative sign in eqn. 2 depicts that the layer modulus is a resistance of a 2D material to - $\mathcal{F}$

Figure 1 Illustration of force per unit length.

In this work we considered a stretching force.

From the work of Andrew and co-works in their PRB 2010 (Andrew, *et.al*, 2012), they indicated that the layer modulus (γ_o) of a monolayer graphitic material can be estimated by the in-plane linear modulus using the eqn. 3 below

$$\gamma_o = \frac{t\beta_o}{2} \qquad\qquad 3$$

Whereβ_o, is a linear modulus with respect to bulk pressure and t is the layer thickness.

Andrew and co-workers went ahead and indicated the possibility of obtaining a 2D EOS relating the force applied$\mathcal{F}$, to the surface area of any 2D material as

$$\mathcal{F} = -2\gamma_o\left\{\epsilon + (1-\acute{\gamma_o})\epsilon^2 + \frac{2}{3}[(1-\acute{\gamma_o}) + \gamma_o\ddot{\gamma_o}]\epsilon^2\right\} \qquad 4$$

Where $\epsilon = \frac{1}{2}\left[1 - \frac{A_0}{A}\right]$ and is known as the equibiaxial Eulerian strain.

$A_0, \gamma_o, \acute{\gamma_o}$ and $\ddot{\gamma_o}$ are the optimized values of unit cell area, layer modulus, the force per unit length derivative and second derivative of the layer modulus at $\mathcal{F} = o$

From eqn.1 it implies that $E = \int \mathcal{F}\, \partial A$ then we can integrate eqn.4 to get energy equation of state as

$$E(A) = E_o + 4A_0\gamma_o\left[\frac{1}{2}\epsilon^2 + \frac{1}{3}(5-\acute{\gamma_o})\epsilon^3 + \frac{1}{6}[(1-\acute{\gamma_o})(8-\acute{\gamma_o})+\gamma_o\ddot{\gamma_o} + 18]\epsilon^4\right] \qquad 5$$

Which can be fitted to hydrostatic expansion and compression date to extract $A_0, \gamma_o, \acute{\gamma_o}$ and $\ddot{\gamma_o}$.

2. Computational Details

All calculations were done within the framework of Density-Functional Theory (DFT) (Hohenberg & Kohn, 1964), using the Projector Augmented Wave (PAW) (Blochi, 1994), formalism as implemented in quantum expresso code (Giannozzi, et al., 2009). We used Pardew-Burke-Ernzerhef (PBE) Generalized Gradient Approximation (Perdew, Burke, & Ernzehof, 1996) exchange correction. The K-point sampling was done at 12 12 1 Monkhorst-Park (Monkhorst & Pack, 1976) and each structure was relaxed so that the forces converged to 0.01eV/Å. In all cases the kinetic energy cut off of 55Ry was used. A height of 20 Å was used in order to prevent spurious interactions between unit cells repeating perpendicular to the layer plane.

3. Results and Discussion

In this study we considered graphene, BN and a number of newly synthesized Janus which include WS_2, WSSe, WSe_2, MoS_2, MoSSe and $MoSe_2$. The lattice parameters are arranged in table one in an increasing order, with the Janus having a higher value of a= 3.189 Å, 3.247 Å, .3.2.97 Å, 3.187 Å, 3.256 Å and 3.331 Å for WS_2, WSSe, WSe_2, MoS_2, MoSSe and $MoSe_2$ respectively.

The values of *a* is higher when the transitional metal is combined with Se chalcogen atom than S. This is due to higher molecular mass of Se as compared to S. It can also be seen that the lattice constant a increases in the series $MS_2 < MSSe < MSe_2$ (M=Mo,W) since as sulphur is substituted with Se , the number of electron increases thus high repulsive force that leads to increase in the lattice distance. The relaxed honeycomb structure of graphene has unit cell with lattice constant of 2.467 Å and BN of 2.515 Å, which combers well with values obtained by reference (Andrew, *et.al,* 2012). The lattice parameters of the Janus is generally high than graphene and BN due to increasing in the number of atoms in the structure of the molecule.

EOS fit parameters of equilibrium, layer modulus γ_o = 206.7 N/m, 177.3N/m force per unit length derivative , $\dot{\gamma_o}$ = 4.338N/m, 4.414N/m double force per unit length derivative $\ddot{\gamma_o}$ = −0.0306 N/m, -0.034N/m for graphene and BN respectively. The higher layer modulus value indicates the material are more resilient to stretching thus maintains its structure properties when changing form 3D to 2D state. The resilience to stretching in Janus is low as listed in the table 1 below. Generally a transitional metal bonded to Se chalcogen atom is less resilient the when bonded to S atom.

TABLE I.

	A_0	a	γ_0	γ_0'	γ_0''	Bs	A_f
Graphene	5.271	2.467	206.6	4.368	-0.034	31.5	27.27
BN	5.479	2.515	177.3	4.414	-0.034	27.7	28.9
WS_2	8.807	3.189	110.8	4.301	-0.052	17.8	47.1
WSSe	9.134	3.247	101.6	4.378	-0.053	16.4	49.4
MoS_2	8.796	3.187	100.9	4.311	-0.065	16.0	46.6
WSe_2	9.413	3.297	93.3	4.454	-0.054	15.1	51.5
MoSSe	9.184	3.256	92.8	4.379	-0.062	14.7	49.0
$MoSe_2$	9.610	3.331	85.2	4.408	-0.065	13.6	51.7

References

Andrew, R., Mapesha, E., Ukpong, A. M., & Chetty, N. (2012). Mechanical properties of graphene and boronitrene. *American Physical Society, 85*, 125428-125437.

Blochi, P. (1994). Projector Augmented Wave methods. *Physical Review, 50*, 17953.

Chhowalla, M., Shin, S., Eda, G., Li, J., Loh, K., & Zhang, H. (2013). The chemistry of two-dimensional layered transition metal dichalcogenide nanosheets. *Natire chemisty., 5*, 263-275.

Duan, X., Wang, C., Shaw, J., Cheng, R., Chen, Y., Li, H., . . . Duan, X. (2014). Lateral epitaxial growth of two-dimensional layered semiconductor heterojunctions. *Nature Nanotechnology, 9*, pages 1024–1030.

Geim, K. (2009). Graphene: Status and Prospects. *Science, 324*, 1530-1534.

Giannozzi, P., Baroni, S., Baonini , N., Calandra, M., Car, R., & Cavazzoni, C. (2009). QUANTUM EXPRESSO: A modular and open source softwere project for quantum simulations of materials. *Physicaal Condensed Matter, 21*, 395502.

Hohenberg, P., & Kohn, W. (1964). Inhomogeneous electron gas. *Physical Review, 136*, 864-871.

Li, M., Shi, Y., Cheng, C., Lu, L., Lin, Y., Tang, H., & Tsai, M. (2015). Epitaxial growth of a monolayer WSe2-MoS2 lateral p-n junction with an atomically sharp interface. *Science, 349*, 524-528.

Liu, K., & Wu, J. (2015). Journal of materials Research Mechanical properties os 2D Metarials and heterostuctures. *Journal of materials research, 31*, 822-844.

Lu, A., Zhu, H., Xiao, J., Chuu, C., Han, Y., Ming, C., . . . Yang, Y. (2017). Janus monolayers of transition metal dichalcogenides. *Nature Nanotechnology, 12*, 744–749.

Ma, X., Wu, X., Wang, H., & Wang, Y. (2018). A Janus MoSSe monolayer: a potential wide solar-spectrum water-splitting photocatalyst with a low carrier recombination rate. *material chemistry A, 6*, 2295-2301.

Monkhorst, H., & Pack, J. (1976). Special points for brillion-zone intergrations. *Phyical Review, 13*, 5188.

Novoselov, K., Geim, K., Movozov, S., Jiang, D., Ziang, X., Dubonos, S., . . . Firsov, A. (2004). Electric field Effect in Atomically Thin carbon Films. *Science, 306*, 666-669.

Perdew, P., Burke, K., & Ernzehof, M. (1996). generalised Gradient Apeoximation made simple. *Physical Review, 77*, 3865.

van der Waals Layered Materials: Opportunities and Challenges. (2017). *American Chemical Society, 11*, 11803-11830.

Yifei, Y., Liqin, S., Shi, H., Lujun, H., Liu, Y., Zhenghe, J., . . . Cao, L. (2015). Equally Efficient Interlayer Exciton Relaxation and Improved Absorption in Epitaxial and Nonepitaxial MoS2/WS2 Heterostructures. *American Chemical Society, 15*, 481-496.

ab Initio Study of Electronic Structure Properties of Lead Halide Perovskites for Optical Performance of Solar Cell

Truphena J. Kipkwarkwar[1*], Philip. W. O Nyawere[2], Christopher.M. Maghanga[1]

[1]Kabarak University, Department of Biological & Physical Sciences,
P.O. Private bag, 20157, Kabarak, Kenya.Tel:+254 710848999,
[*]Email truphenamengich@yahoo.com

[2]Rongo University, Department of Physical Sciences,
P.O. Box 103 – 40404, Rongo, Kenya.Tel:+254 728342054,

Abstract

The ever increasing demand of energy has necessitated the need of coming up with measures of seeking alternative energy sources. Solar energy is one of the most important alternative sources of energy. However,the use of the first and second generations solar cells made of silicon in making solar panels has notable shortcomings such as unaffordability and lack of longevity of the electric power generated. In this regard, therefore, We report the initial electronic structure results of lead halide perovskite (APbX3) where (X = I/Br/Cl and A=CH_3NH_3/$CH(NH_2)_2^+$/Cs^+) for application in solar cells. Calculations were done using density functional theory within generalized gradient (GGA) approximations, Projector augmented wave (PAW) pseudopotentials of the functional type Perdew-Burke-Ernzerhof (PBE).The calculated lattice parameter for $CH_3NH_3PbI_3$ is foundto be 6.27Å which compares relatively well with experimental value. Our band gap is 1.74 eV and is underestimated as expected. Understanding these electronic structure properties are critical in application of this material in optoelectronics.

Key words: Perovskites, halides, electronic structure, optoelectronics.

1.0 Introduction

The general formula of lead halide perovskites is $APbX_3$ where A represents an organic positively charged ion ($CH_3NH_3^+$; $CH(NH_2)_2^+$) or an inorganic cation (Cs^+) and X represents a halide such as Iodide (I^+), Bromide (Br^-), or Chloride (Cl^-). The electronic structure is as shown in Fig 1.
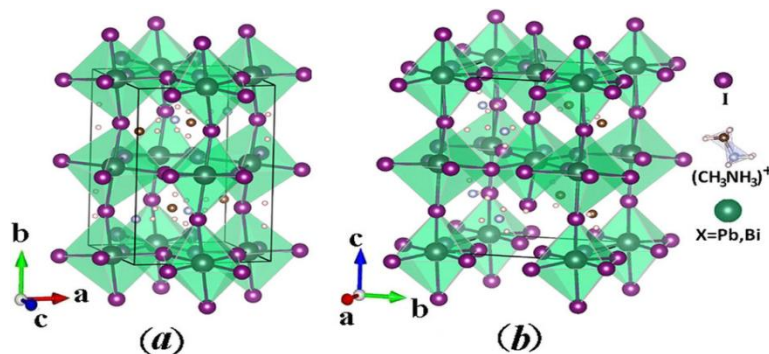

(a) *(b)*

Figure 1: Electronic Structure of Lead Halide Perovskite (Zhu & Liu, 2016)

(Saliba *et al.,* 2016) stated that lead halide perovskites have become popular as photovoltaic materials due to their high power conversion efficiency (PCE). The PCE of the aforesaid perovskites is over 22%. According to (Miyata *et a.l,* 2017), lead halide perovskites shows great deal of defect tolerance due to their excellent optoelectronic properties.The lead halide perovskites are likely not to have mechanistic limitations in relation to charge carrier protection and mobility.

The growing need of electrical energy has made it imperative to devise measures of seeking alternative energy sources. One of the crucial alternative sources of electrical energy is solar energy. However, the upto this time, the use of the first and second generations solar cells made of silicon in making solar panels has various shortcomings. These include unaffordability and lack of longevity of the electric power generated by the solar energy (Manser *et al.,* 2016). The mentioned attributes imply that the solar energy so produced is relatively expensive and its sustainability cannot be guaranteed with precision. In this regard, therefore, it becomes imperative to conduct further analysis particularly in respect to third generation solar cells with the view of improving both durability and longevity. There is limited literature regarding lead halide perovskites. This necessitates an empirical study to analyze the electronic properties of lead halide perovskites in relation to optical performance of lead halide perovskite. The study seeks to examine the electronic properties with the view of finding ways of improving them in respect to optical performance. Moreover, the study intends to find ways in which the identified properties can enhance durability and efficiency of lead halide perovskite.

2.0Theory

(Phillppe *et al.,* (2015) conducted a photoelectron spectroscopy investigation on the chemical and electronic structure characterization of lead halide perovskites and also their stability behaviour under varied exposures. The study noted that there are hitherto two perovskite materials which have drawn a lot of interest in relation to solar cells. These materials are $CH_3NH_3PbI_3$ and $CH_3NH_3PbI_{3-x}Cl_x$. The study noted that photoelectron spectroscopy (PES) has the capacity to provide a generalized picture of the electronic structure of the perovskite and the relation of the same to mesoporous TiO_2 when studied with hard X-rays. It was further found that both $CH_3NH_3PbI_3$ and $CH_3NH_3PbI_{3-x}Cl_x$ exhibit very close electronic structure in spite of having very different morphologies and kinetics of formation.

A study conducted by (Pazoki *et al.,* 2017) analyzed the electronic structure of organic-inorganic lanthanide iodide perovskite solar cell materials. The electronic structure of various lanthanide-based materials investigated in the study had not been explored previously in the context of metalorganic halide perovskites. The study revealed that the localized f-electrons within the DFT+U approach make the dominant electronic contribution to the states are found atop the valence band. This results in a strong influence on the photo-physical properties of the lanthanide perovskites. This meant that the primary valence to conduction band electronic transition for $MAEuI_3$ is premised on inner shell f-electron localized states in a periodic framework of perovskite crystals. In different circumstances, the onset of optical absorption would be inert in respect to quantum confinement effects.

Similarly, Takaba, Kimura and Alam (2017) conducted a study on crystal and electronic structure of substituted halide perovskites with closer focus on density functional calculations and molecular dynamics. The study was premised on the acknowledgement that durability of organo-lead halide perovskite is paramount due to its practical application in solar cells. The study was guided by density functional theory (DFT) and molecular dynamics to investigate among others, electronic structure of partially substituted cubic $MA_{0.5}X_{0.5}PbI_3$ ($MA = CH_3NH_3^+$, $X = NH_4^+$ or $(NH_2)_2CH^+$ or Cs^+). The results of pertinent calculation indicated that a partial substitution on MA led to a lattice distortion. Consequently MA or X are prevented from the diffusion between A sites in the perovskite. More so, the calculations of DFT indicated that the electronic structures of the studied partially substituted perovskites were similar with that of $MAPbI_3$.

The size of the electronic band gap of a material is very critical for it to be used as solar cell absorbers since an appropriate band gap is required in the absorption of the photons located in the infrared region of the solar spectrum. The nature of the band gap assists in the estimation of the amount of light absorbed in the maximizing the efficiency of the solar cell with minimum optical losses(Mayengbam *et al.,*2018). Its therefore clear that the efficiency of a solar cell depends on the band gap of the material. It is for this reason that the electronic properties of $CH_3NH_3PbI_3$ are investigated with an aim of improving itsefficiencyfor use in solar cell.

3.0 Methodology

All calculations of relaxation, optimization and elastic constants were done within the Density Functional Theory implemented in the Quantum ESPRESSO (Giannozzi *et al*., 2009). This is done by employing for the exchange-correlation functional, the generalized gradient approximation (GGA) of Perdew-Burke-Ernzerhof (PBE) and (PBE-sol) functional type (Perdew *et al.,* 1996) and Projector augmented wave (PAW) pseudo-potentials. Pseudopotentials were obtained from the Quantum-Espresso website(Giannozzi *et al*., 2009).The convergence test for plane-wave energy cut off and the k-point grid(7 x7 x7) was determined and the atomic position at fixed lattice constants relaxed at a temperature of 0K. (Beltracchi, 2015). The outermost s, p, and d electrons in (lead)Pb are taken to be the valence electrons whose interactions with the remaining ions is modeled by pseudopotentials generated within the projector-augmented wave (PAW) (Tao *et al.,*2017)The total energy convergence in the iterative solution of the Kohn-Sham equations was fixed at $2x10^8$Rydberge (Ry) (Nyawere *et al.,*2014).

4.0 Results and discussions

This is a very significant principle in any DFT calculation. The convergence of the cut-off energy with respect to the total energy was found at 30 Ry and is shown in Fig 1.
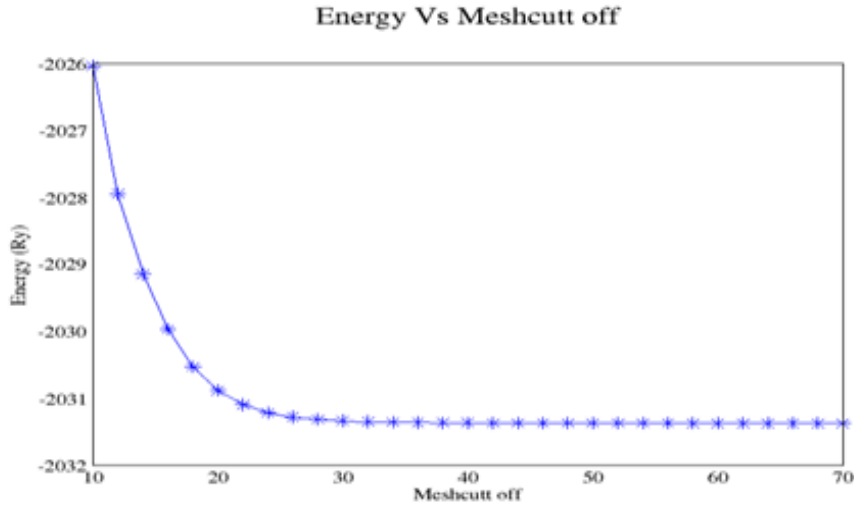
Fig 1: **convergence of Energy with the plane wave cut-off**

This shows that cut-off energy below 30Ry is inadequate. Therefore, one must select values greater than 30 Ry so as to obtain more precise results.

Convergence test for k-points was done and the results are as shown in Fig 2 below. The appropriate k-point mesh was taken at 7x7x7. Increase in the mesh consumes more computational time with no much difference.
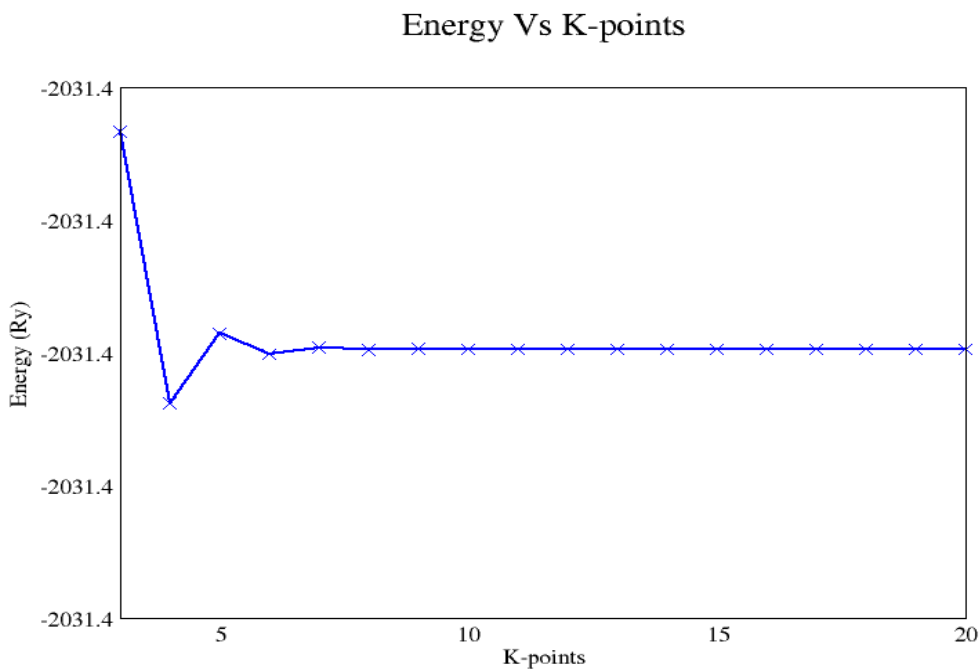
Fig 2: Convergence of total energy with k-point

The resulting total energies of the system and the volumes of the unit cell were applied to the Murnaghan equation of state (EOS) (Murnaghan, 1944), to get the equilibrium volume and bulk modulus.
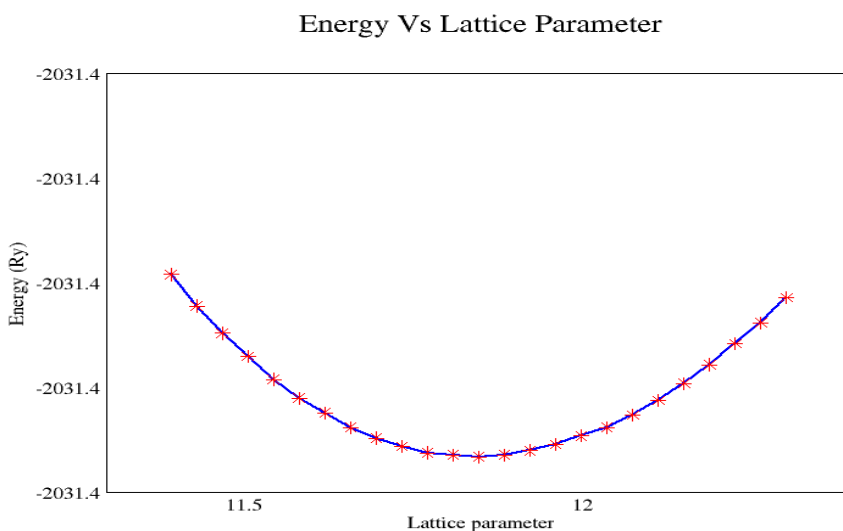

Fig 3:

Total energy Vs Lattice parameter

The lattice parameter was obtained to be 6.27Åwhich is equal to 11.85 Bohr as illustrated in Fig 3above.

Table 1: Calculated lattice parameter a (Å) of $CH_3NH_3PbI_3$ and volume (Å)^3 from this study compared with other work.

	a(Å)	Volume (Å)^3
This work	6.27	246.451
(Stoump *et al.,*2013)	6.31	251.240

	6.46	269.586
(Brivio *et al.,* 2013)		
	6.31	251.240
(Feng& Ciao, 2014)		
Ref.4 (Brivio *et al.,*2014)	6.28	247.673

Density of states calculations are shown in Fig 5. This shows that band gap of the optimized structures of $CH_3NH_3PbI_3$ is 1.74 eV without considering the spin orbit coupling (SOC). This band gap is in agreement with other theoretical values of other studies. The comparative results are shown Table 2. It is a well know fact that PBE pseudopotentials under estimates band gaps.Understanding band gap will enable us study the optical gap and other optical properties of $CH_3NH_3PbI_3$ and their photovoltaic applications.
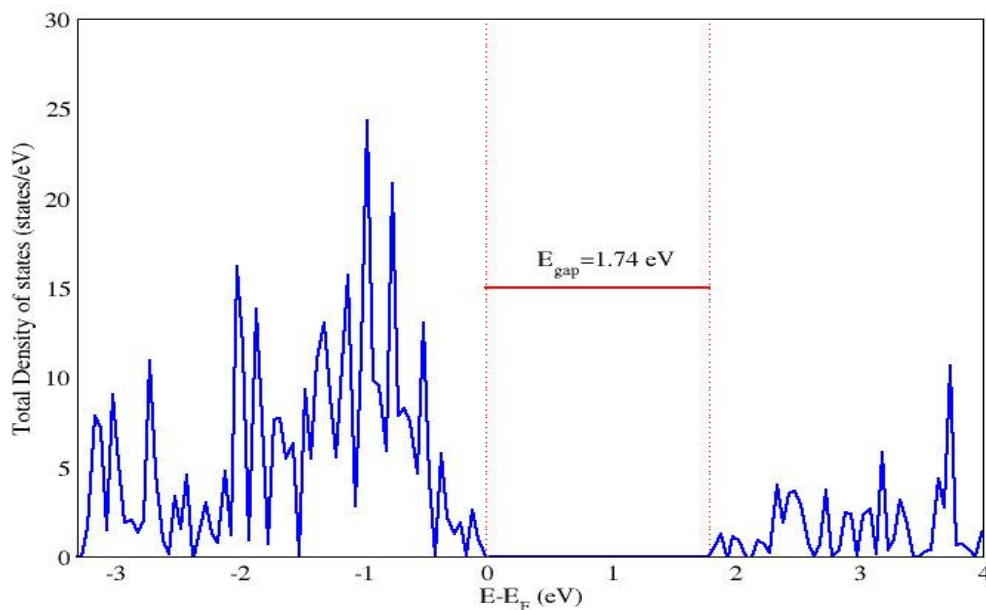

Fig 5: Total Density of States Vs Energy

Calculation of the bands was done and results presented in figure 6.It was observed that the gap was direct at the gamma point R.$CH_3NH_3PbI_3$ has a gap of 1.74eV.The top of the valence band and the bottom was dominated by Iodine orbitals.The direct gap is suitable for photo absorption since its signature for most optical materials.
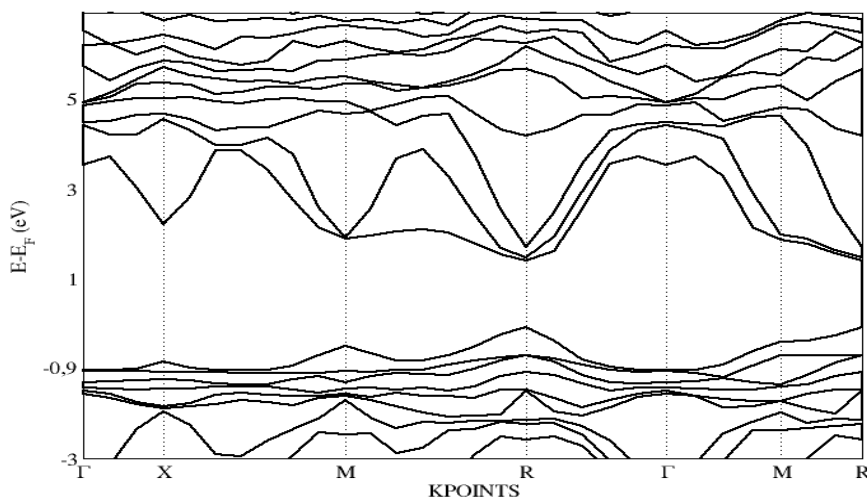
Fig 6: Band structure of **CH$_3$NH$_3$PbI$_3$**

Table 2: Value of Calculated without SOC Band gap of CH$_3$ NH$_3$PbI$_3$ in comparison with other studies

This work	(Brivio *et al.,*2014)	(Yamanda *et al.,*2014)	(Jishi *et al.,*2014)
QE	GW	Exp	WIEN2k code
1.74eV	2.73eV	1.61eV	1.54eV

5.0 Conclusions

The calculations on electronic structure of CH$_3$NH$_3$PbI$_3$ have been reported. The lattice parameter, density of states and band gap was determined. These parameters are in agreement with both experimental and other theoretical computations so far done on CH$_3$NH$_3$PbI$_3$.Its clear from the results obtained that CH$_3$NH$_3$PbI$_3$ has a small band gap which is requirement for any solar cell material.The the correct optimized lattice parameter was obtained which is dependent on the value of band gap energy.With these initial parameters in place, optical properties can be estimated.

Acknowledgement

References

Beltracchi, P. (2015). *First-principles study of hybrid organic-inorganic perovskites for photovoltaic applications, A* (Doctoral dissertation, Colorado School of Mines. Arthur Lakes Library) 1-58.

Brivio, F., Butler, K. T., Walsh, A., & Van Schilfgaarde, M. (2014). Relativistic

quasiparticle self-consistent electronic structure of hybrid halide perovskite photovoltaic absorbers. *Physical Review B*, *89*(15), 155204.

Feng, J. (2014). Mechanical properties of hybrid organic-inorganic $CH_3NH_3BX_3$ (B = Sn, Pb; X = Br, I) perovskites used in solar cell absorbers. *APL Materials,2*(8), 081801.

Giannozzi P., Baroni S., Bonini N., Calandra M., Car R., Cavazzoni C., Ceresoli D., Chiarotti, G. Cococcioni L. M., Dabo I., Dal Corso A., Fabris S., Fratesi G., de Gironcoli S., Gebauer R., Gerstmann U., Gougoussis C., Kokalj A., Lazzeri M.(2009).Quantum ESPRESSO: a modular and open-source software project for quantum simulations of materials. *Journal of Physics: Condensed Matter, 21*, 395502

Jishi, R. A., Ta, O. B., & Sharif, A. A. (2014). Modeling of lead halide perovskites for photovoltaic applications. *The Journal of Physical Chemistry C*, *118*(49), 28344-28349.

Manser, J.S., Saidaminov, M.I., Christians, J.A., Bakr, O.M., & Kamat, P.V. (2016). Lead halide perovskites for solar energy conversion. *Accounts of Chemical Research, 49*, 330-338.

Mayengbam, R., Tripathy, S. K., & Palai, G. (2018). First-Principle Insights of Electronicand Optical Properties of Cubic Organic–Inorganic MAGe x Pb (1–x) I3 Perovskites for Photovoltaic Applications. *The Journal of Physical Chemistry C*, *122*(49), 28245-28255.

Miyata, K., Meggiolaro, D., Trinh, M.T., Joshi, P.P., Mosconi, E., Jones,S.C., Angelis, F., & Zhu, X.Y. (2017). Large polarons in lead halide perovskites. *Science Advances,3*(8).Access on November 4,2017 from .Org/content/3/8e1701217

Nyawere, P. W. O., Makau, N. W., & Amolo, G. O. (2014). Ab initio Calculations of Properties of Orthorhombic Phase of BaF2.

Pazoki, M., Rockert, A., Wolf, M.J., Imani, R., Edvinsson, T., &Kullgren, J. (2017). Electronic structure of organic-inorganic lanthanide iodide perovskite solar cell materials. *Journal of Materials Chemistry*, 44, 22837-23384.

Perdew, J. P., Burke, K., & Ernzerhof, M. (1996). Generalized gradient approximation made simple. *Physical review letters, 77*(18), 386

Phillppe, B., Park, B., Lindblad, R., &Rensmo, H. (2015). Chemical and electronic structure characterization of lead halide perovskites and stability behavior under different exposures – a photoelectron spectroscopy investigation. *Chem. Mater.*, *27* (5),1720–1731.

Stamplecoskie, K.G., Manser, J.S., &Kamat, P.V. (2015). Dual nature of the excited state in organic−inorganic lead halide perovskites. *Energy Environ. Sci., 8,* 208−215.

Takaba, H., Kimura, S., &Alam, K. (2017). Crystal and electronic structures of substituted halide perovskites based n density functional calculation and molecular dynamics. *Journal of Chemical Physics,* 485/486, 22-28.

Tao, S.X., Cao, X., &Bobbert, P.A. (2017). Accurate and efficient band gap predictions of metal halide perovskites using the DFT-1/2 method: GW accuracy with DFT expense. *Scientific Reports, 7*, 14386.

Yamada, Y., Nakamura, T., Endo, M., Wakamiya, A., & Kanemitsu, Y. (2014). Near-band-edge optical responses of solution-processed organic–inorganic hybrid perovskite CH3NH3PbI3 on mesoporous TiO_2electrodes. *Applied Physics Express*, *7*(3), 032302.

Zhu, H. X., & Liu, J. M. (2016). Electronic structure of organometal halide perovskite CH3 NH3BiI 3 and optical absorption extending to infrared region. *Scientific reports*, *6*, 37425.

Optical Modeling Of Fluorine Doped Tin Oxide Films For Spectrally Selective Applications

Isoe Wycliffe M [1,*], Maxwell J.Mageto[1] C. M. Maghanga[2] and M Mghendi[3]

[1]Department of Physics, Masinde Muliro University of Science and Technology, P.O. Box 190 Kakamega, Kenya

Tel: +254 0739 631 749, *Email: isoewycliffe@gmail.com

[2]Department of Physical & Biological Sciences, Kabarak University, P.O. Box Private Bag Kabarak, Nakuru, Kenya.
Tel: +254 0733 938 470, Email: CMaghanga@kabarak.ac.ke

[3]Department of Physics, University of Eldoret, P.O. Box 1125-30100, Eldoret
Email: mghendi@gmail.com

Abstract

SnO_2: F films are widely used for solar cell applications as the front electrode as well as other applications such as electrochromics and displays. Optical design of these and other applications need the knowledge of optical constants. In this study we used the dielectric constant of a combined Drude and Lorentz to model the optical behavior of SnO_2: F. To do this, we used the fitting parameters from existing literature. From the model we got n and k values which we inserted into Fresnel R and T calculator and computed R and T spectra over the 300nm -2500nm wavelength range using Fresnel's equations. We plotted n, k, T and R for different values of plasma frequency, ω_p and damping parameter, Γ. The films exhibited very high visual transmittance and high infrared reflectance. The results implied the possibleness of the films to be employed as spectrally selective coating materials.

KEY WORDS: Optical constants, damping parameter, thin film, Drude-Lorentz model.

1. Introduction

Transparent conductors are materials that possess both good electrical conductivity and optical transparency in the visible portion of the electromagnetic spectrum. A wide band gap (~>3 eV) is needed for visible transparency. A combination of transparency and conduction can be achieved in two different types of materials[1]:- (1) Extremely thin films of metals especially Ag, Au or Cu on glass or (2) among wide-band gap oxide semiconductors such as fluorine-doped tin oxide (FTO), antimony-doped tin oxide (ATO), tin-doped indium–oxide (ITO), niobium- doped titanium oxide (TNO) and aluminium-doped zinc oxide (AZO).Wide-band gap oxide semiconductors are in most cases referred as transparent conducting oxides (TCOs).

TCOs have been employed technologically for more than a half-century in applications requiring both high conductivity and optical transparency. Some TCO applications include transparent electrodes for flat-panel displays[2], liquid crystal displays (LCDs)[3], organic light-emitting diodes (OLEDs)[4], as coatings for heat reflective windows i.e. thermal management for window glass[5], electrochromic (smart) windows[6], solar cells[7], electromagnetic shielding[8],

functional glasses[9], electrochemical cells[10] and gas sensors[11]. TCOs are also applicable to transparent optoelectronics because they have the unique features of optical transparency in the visible region and controllable electrical conductivity, from almost insulating to degenerate semi-conducting ($\sim 10^4$ S/cm) behaviour.

Tin oxide, among the semiconductors, demonstrates special features in chemical inertness [12], stability to heat treatment and mechanical hardness[13]. Further, tin oxide films are highly transparent in the visible range [14]. It also has a direct band gap of approximately 3.6eV[15] which makes it possible to have a wide range of applications in electronic devices. In order to improve its optical and electrical properties, tin oxide films need to be doped with the right dopants such as fluorine, cadmium, molybdenum and antimony[16]. Among these dopants fluorine is found to be the best dopant for tin oxide since the radii of O^{2-} and F^- are similar hence there will be no mismatch of lattices during doping[16].

Thin films of transparent oxide semiconductors, such as F-doped tin oxide, are widely investigated due to their high optical transmission, electrical conduction, and infrared reflection. These properties make these films to find wide applications in optoelectronic devices, hybrid microelectronics, photo thermal conversion and direct energy conversion devices particularly in conductor-insulator- semiconductor solar cells. Fluorine-doped tin oxide has a work function of about 4.9eV, electron concentration in the order of $10^{20} cm^{-3}$, an approximate minimum resistivity of about $200\mu\Omega cm$ and a visible absorption coefficient of about 0.04[17].

Thin film surface coatings are most widely employed for the efficient conversion of solar radiation into other useful forms, such as thermal energy for heating and cooling applications; and electrical energy by direct conversion using photovoltaic cells. The other current applications of such optical coatings include: transparent heat mirrors[18], antireflection coatings[19], architectural coatings[20], photo-thermal converters[20], and photo- catalysis[21].

Invar Hamberg (1984) in his thesis[22], reported that for the material to be used as spectrally selective coating material, it must meet three conditions: (1) should have a significantly wide band gap in order for the material to guarantee the key absorption edge to be below a solar wavelength length of approximately 300nm; (2) a prospect to dope the material to attain a high free carrier concentration leading to a high infrared reflectivity; (3) a limited absorption between the key absorption edge and the plasma wavelength, to guarantee a high luminous transmittance. Also, MghendiMwamburi in his thesis[23] reported separately that for a material to be used as spectrally selective reflector (SSR)it must exhibit very high visual transmittance and high infrared reflectance. Furthermore, he suggested that the region of the plasma absorption peak must be positioned in the part of the solar spectrum with photon energies lower than the band gap of the given solar cell. Spectrally selective films are those that allow peculiarly selected portions of light spectrum to pass through a medium while blocking some i.e. their transmission and/or reflection properties are regulated for selected and controlled packages of thermal radiation fluxes[24]. The conditions aforementioned necessitated the need to investigate a thin film that would meet all the conditions. The aim of the study was to model SSR films.

There are apparently many methods that have been employed to study the optical behavior of SnO_2: F films as it is the case in numerous publications. The appropriate investigation of the optical properties of the films requires the finding of optical constants such like the extinction coefficient, k and refractive index, n over the desired wavelength range. In the present work we

employed the dielectric constant of a combined Drude and Lorentz to investigate the optical properties of SnO_2: F films.

1.1 Theoretical Background

The absorption and refraction of a medium can be described by a single quantity called complex refractive index[25]. This is usually given the symbol $\tilde{n}$ or N and is defined as shown in equation (1).

$$N = n + ik \qquad [1]$$

The real part of N namely n is the same as the normal refractive index defined in equation (2). The imaginary part of N, namely k, is called the extinction coefficient which is related with absorption coefficient by equation (3).

$$n = \frac{c}{v} \qquad [2]$$

$$\alpha = \frac{2\omega k}{c} = \frac{4\pi k}{\lambda} \qquad [3]$$

We can relate the complex refractive index of any medium to complex dielectric constant by using equation 4. This shows us that if n is complex, then ε must also be complex.

$$N^2 = \tilde{\varepsilon}_r = \varepsilon_1 + i\varepsilon_2 \qquad [4]$$

By comparing equations (1) and (4), explicit relationships between the real and imaginary parts of N and $\tilde{\varepsilon}$ can be computed and the resulting equations are as shown in equations (5) and (6).

$$\varepsilon_1 = n^2 - k^2 \qquad [5]$$

$$\varepsilon_2 = 2nk \qquad [6]$$

Here n, k, ε_1 and ε_2 are referred to as the optical 'constants' of the medium. They are referred to as constants due to historical reasons otherwise they are functions of wavelength. ε_1 is related to the polarizability and ε_2 to the true optical absorption. These values depend on the photon energy, $E = \hbar\omega$. Further, these optical constants, for any medium, can calculated from a Drude-Lorentz model given in equation (7). The individual Drude and Lorentz models are as given in equations (8) and (9) respectively.

$$\varepsilon = \varepsilon_\infty - \frac{\omega_D^2}{\omega^2 + i\Gamma_D\omega} + \frac{\omega_L^2}{\left(\omega_0^2 - \omega^2\right) - i\omega\Gamma_L} \qquad [7]$$

$$\varepsilon_r'(\omega) = 1 - \omega_p^2 \cdot \frac{1}{\omega^2 + \Gamma^2}, \qquad \varepsilon_r''(\omega) = \omega_p^2 \frac{\Gamma/\omega}{\omega^2 + \Gamma^2} \qquad [8]$$

$$\tilde{\varepsilon} = 1 + \frac{Ne^2}{\varepsilon_0 m} \frac{1}{\left(\omega_0^2 - \omega^2\right) - i\omega\Gamma} \qquad [9]$$

The Fresnel equations that are usually used to work out the transmittance and reflectance of the films are as shown in equations 10-19[26].

$$t_p = \frac{2N_1\cos\theta_1}{N_1\cos\theta_2 + N_2\cos\theta_1} \qquad [10]$$

$$t_s = \frac{2N_1\cos\theta_1}{N_1\cos\theta_1 + N_2\cos\theta_2} \qquad [11]$$

$$r_p = \frac{N_2\cos\theta_1 - N_1\cos\theta_2}{N_2\cos\theta_1 + N_1\cos\theta_2} \qquad [12]$$

$$r_s = \frac{N_1\cos\theta_1 - N_2\cos\theta_2}{N_1\cos\theta_1 + N_2\cos\theta_2} \qquad [13]$$

And at normal incidence the equations become:

$$r_1 = \frac{N_2 - N_1}{N_2 + N_1}, \ r_2 = \frac{N_3 - N_2}{N_3 + N_2} \qquad [14]$$

$$t_1 = \frac{2}{N_1 + N_2}, \ t_2 = \frac{2N_2}{N_2 + N_3} \qquad [15]$$

Hence, we can find r and t according to:

$$r = \frac{r_1 + r_2 e^{-2i\partial}}{1 + r_1 r_2 e^{-2i\partial}} \qquad [16]$$

$$t = \frac{t_1 t_2 e^{-i\partial}}{1 + r_1 r_2 e^{-2i\partial}} \qquad [17]$$

where the phase shift, ∂, is given by

$$\partial = -\frac{2\pi}{\lambda} N_2 d\cos\theta_2, \text{ which for normal incidence becomes; } \partial = -\frac{2\pi N_2}{\lambda} d \qquad [18]$$

and r_1 and t_1 are the Fresnel coefficients for the boundary between air and film and r_2 and t_2 are the corresponding coefficients for the boundary between film and substrate.

With the Fresnel equations above we can calculate the intensity reflectance, R, and the intensity transmittance, T, according to:

$$R = rr^* \qquad \text{and} \qquad T = \text{Re}\left(\frac{N_3}{N_1}\right) tt^* \qquad [19]$$

where r^* is the conjugate of the amplitude reflectance and t^* is the conjugate of the amplitude transmittance.

2. The Simulation Method.

The Drude–Lorentz modeling of optical spectral of SnO_2: F films was simulated using equation (7) with a commercial MATLAB computer program. To do this, we used the fitting parameters from existing literature shown in table (1) which we inserted into the MATLAB program and got n and k values as well as real part (ε_1) and imaginary part (ε_2). We inserted each pair of n and k values into Fresnel equation R & T calculator together with Fresnel's equations (equations 10-19) to compute R- and T- spectra of SnO_2: F films at different film thicknesses, d and for the various doping concentrations, n_e, over $300 - 2500nm$ wavelength range. We used different values of plasma frequencies, $\omega_p\left(s^{-1}\right)$ shown in table 2. All the simulation was done by using the commercial MATLAB computer program

The figures shown below represent the modeled optical data for the different samples i.e. S_A, S_B, S_C, S_D, S_E, S_F and S_G. S_A is the undoped sample whereas S_G is the heavily doped sample. The dopant concentration was increased gradually by varying the value of $\omega_p\left(s^{-1}\right)$ as depicted in table 2.

Table 1. Drude and Lorentz parameters for undoped and F-doped tin oxide

	ε_∞	$\omega_p\left(\times`10^{14}s^{-1}\right)$	$\Gamma_D(eV)$	$\omega_p\left(s^{-1}\right)$	$\Gamma_L(eV)$	$\omega\left(s^{-1}\right)$
SnO₂	4.0	-	-	$1.56\times`10^{14}$	0.5064	$8.19\times`10^{14}$
SnO₂: F	3.19	1.43	0.167	$24.67\times`10^{15}$	0.1275	$1.27\times`10^{15}$

Table 2: Values of plasma frequencies, $\omega_p\left(s^{-1}\right)$ used to calculate the optical constants in a combined Drude and Lorentz model.

Sample	S_A	S_B	S_C	S_D	S_E	S_F	S_G
$\omega_p\left(\times`10^{14}s^{-1}\right)$	0	1.43	2.02	2.85	3.49	4.03	5.71

3. Results and Discussion

3.1 Optical Studies

In order to compare the reflectance and transmittance of SnO_2 thin films with various F-doping levels, the optical R- and T-spectra in the UV-VIS-NIR region of the samples were computed and the results are as shown in Figures 1 (a), (b), (c)and (d). The various film thicknesses shown in figures1 (a), (b) and (c) are meant to magnify the optical properties of the graphs in the near IR for easy comparison.
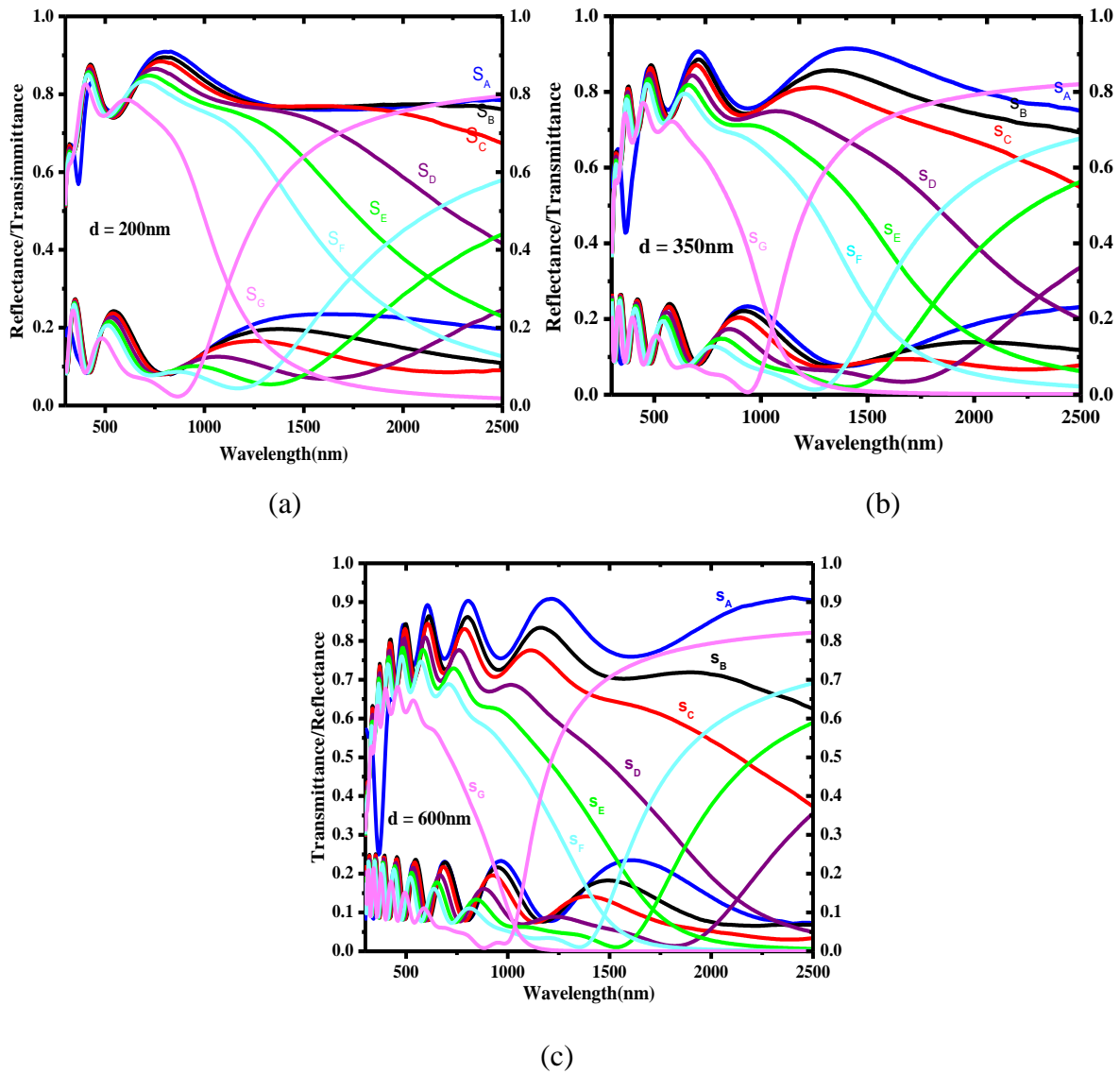
(a)

(b)

(c)

Figure 1 Spectral reflectance and transmittance for various F-doping concentrations at film thickness (a) d = 200nm, (b) d = 350nm, (c) d = 600nm.
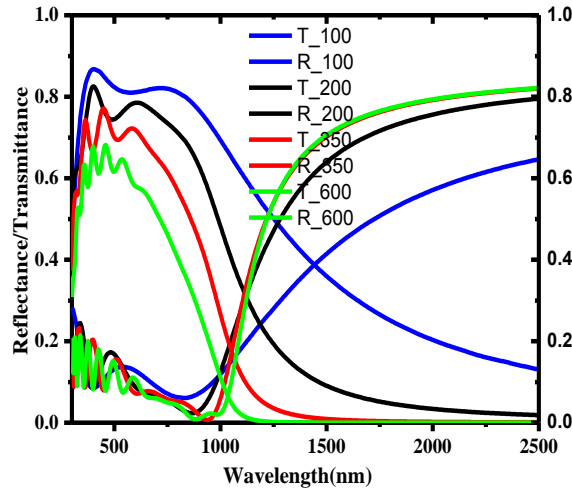
Figure 1(d) Spectral reflectance and transmittance of the highly doped sample (S_G) showing various film thicknesses. The films thicknesses were 100nm, 200nm ,350nm and 600nm.

It was clearly noted from the figures 1 (a), (b) and (c)that the films exhibited high transparency in the visible region but in near IR region the transparency started to decrease with increase in F-doping concentration. The decrease in transmittance is due to reflection by the free electron in the highly F- doped SnO_2. This further illustrates that although doping improves the free carrier concentration thus the conductivity, it jeopardizes the transparency of the film. Thus, there is a demand that a compromise between the optical properties and electrical properties should be attained for TCOs. On the other hand, reflectance increases in the near infrared region with increasing F doping concentration to a maximum of 81.8% for the highly doped sample. The reduction of transmittance and the rise of reflectance at near infrared indicate that the samples start to conduct. These observations are perfectly in agreement with other already reported work[27]. The transmittance and reflectance behavior of the films at various F-doping levels illustrates that doping improves the optical properties as well as conductivity of the films to a significant degree.

The shifts in the transmittance and reflectance fringes of the doped samples proposes that doping leads to a slight change in the thickness and in the refractive index of the films. This can be verified by using the number of interference fringes as given in equation 20[28] and by Swanepoel formula given in equation 21[29]respectively.

$$d = \frac{\lambda_1\lambda_2}{2\left(\lambda_1 n_1 - \lambda_2 n_1\right)} \qquad [20]$$

where n_1 and n_2 are refractive indices at two adjacent maxima (or minima) at λ_1 and λ_2 respectively.

$$n = \sqrt{N + \sqrt{N^2 - S^2}} \qquad [21]$$

where

$$N = 2S\frac{T_M - T_m}{T_M T_m} + \frac{S^2 + 1}{2} \qquad [22]$$

and S is the refractive index of the substrate, T_M and T_m represents the maximum and minimum transmittance envelopes at the fringes.

It was also noted from the figures that there is the cross over between R and T curves which shifts towards the visible range with increasing fluorine doping. These cross over show the position of the plasma wavelength. The plasma frequency ω_p, which according to classical Drude is as given in equation 23, is used to characterize the reflection by the free carriers. Using equation 23 we computed the carrier concentration, n_e of the samples and their corresponding values were recorded as shown in tables 3 and 4.

$$\omega_p = \left(\frac{n_e e^2}{\varepsilon_0 \varepsilon_\infty m^*}\right)^{\frac{1}{2}} \qquad \textbf{[23]}$$

where ε_0 is the permittivity of free space, ε_∞ the high-frequency dielectric constant and m^* the effective conduction –band mass. In this paper we assumed the value of $m^* = 0.25 m_e$ [30] where m_e is the free electron mass.

The Spectral reflectance and transmittance at different film thicknesses were also investigated and the results are as shown in figure 1(d). The film thicknesses were increased from 100nm up to 600nm. It was clearly noted that increasing film thickness leads to an increase in reflectance and a decrease in transmittance. This observation is an evidence that the film thickness significantly affects the transmittance and reflectance characteristics.

The optical constants i.e. spectral refractive index $n(\lambda)$, extinction coefficient $k(\lambda)$, real (ε_1) and imaginary (ε_2) parts of the dielectric constant for SnO_2 and SnO_2 :F films are reported as shown in figures 2 , 3, and 4. From figure 2 it was clear that the undoped film shows a dielectric behavior with n = 2 over the 300nm -2500nm wavelength range. This value is well comparable with 1.98 already reported[13]. This refractive index value makes the transparent semiconducting tin oxide suited to be employed as an inherent antireflection coating on silicon[30].

From figures 3 and 2 it was clearly noted that $k(\lambda)$ increases with increase in wavelength whereas $n(\lambda)$ shows a decrease towards higher wavelengths. These effects are more pronounced with increasing F-doping concentration. This behavior was as expected for the case of metallic materials[31] and it may be associated to both shift of the plasma edge as well as the Burstein-Moss shift of the band edge[32].

Figures 4 show that ε_1 decreases with increasing fluorine doping concentrations while ε_2 shows an increase. It was also clearly noticed that the real dielectric constant, ε_1 is substantially negative in the range of high reflectance. This can be understood to mean that high negative values of ε_1 match with a phase relation between the light and polarization. This relation aligns

the polarization in opposite direction to the incoming electromagnetic wave and hence high reflectance.
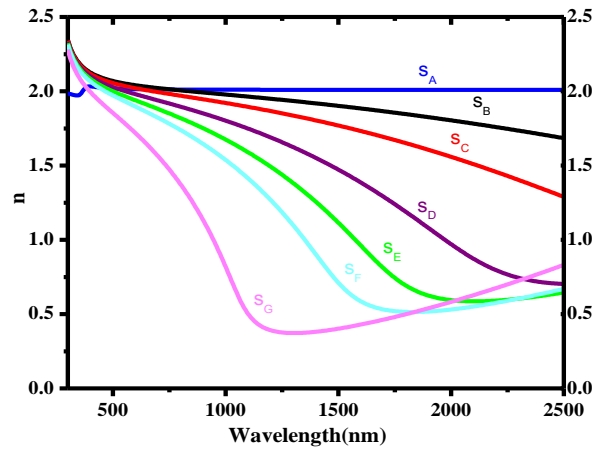

Figure 2. Spectral refractive index, $n(\lambda)$ for the SnO$_2$ and SnO$_2$: F for various levels of F-doping concentration.

Comparing figures 2 and 4(a), it was clearly noted that the real refractive index, n, is small over the region where ε_1 is negative. This makes the material to be optically metal-like[33]. This further informs us that when ε_1 is negative, the optical constants are $n \approx 0$ and $k = \sqrt{-\varepsilon}$ corresponding to an exponentially damped field without energy loss, $\varepsilon_2 = 0$ [34].
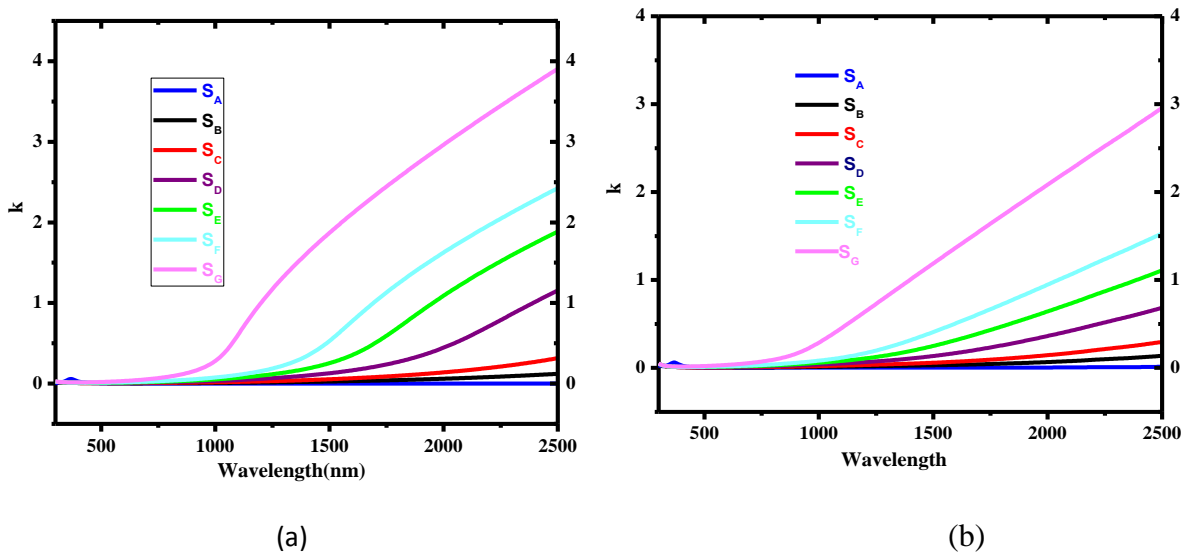

(a)   (b)

Figure 3. Spectral extinction coefficient, $k(\lambda)$ for the SnO$_2$ and SnO$_2$: F showing values of k calculated from (a) Drude-Lorentz model and (b) Hong's formula at d = 350nm.

Figures3 show a comparison of spectral extinction coefficient, $k(\lambda)$ between the various values of k computed from Drude - Lorentz model and that from Hong's formula. The Hong's formula

that was used to compute the k values is as shown in equation 24[35]. The slight difference observed may be due approximation and assumption nature of the formulae.

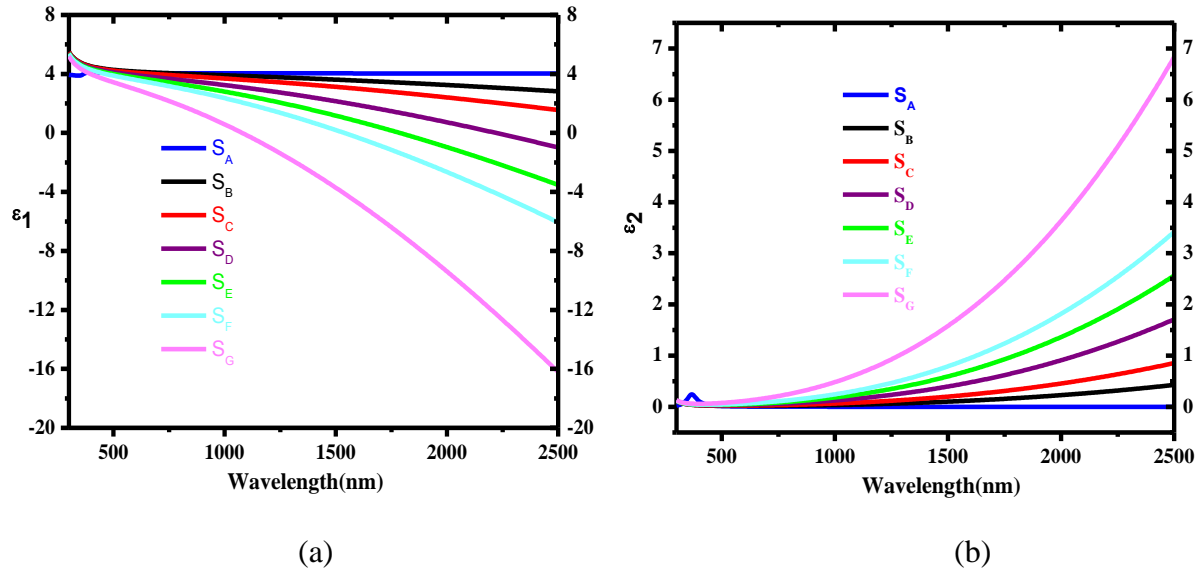$$\frac{1-R}{T} = \exp\left(\frac{4\pi kd}{\lambda}\right) \qquad [24]$$

(a)   (b)

Figure 4. The real part of dielectric constant, ε_1 and the complex dielectric constant, ε_2 verses wavelength.

It can be concluded from the study of optical constants that in practice it is only ε_1 which can be negative.

Table 3: Carrier concentration, n_e values at different plasma frequencies for the samplesat d = 350nm

Sample	Plasma frequency, ω_P $(\times 10^{15} s^{-1})$	Plasma wavelength, λ_P (nm)	Carrier concentration, $(\times 10^{20} cm^{-3})$
S_D	0.81916	2301.08	1.6817
S_E	1.0422	1808.60	2.7223
S_F	1.2354	1525.81	3.8249
S_G	1.7870	1054.84	8.0029

Table 4: Carrier concentration, n_e values at different film thickness.

Thickness d(nm)	Sample	Plasma frequency, ω_P $(\times10^{15}s^{-1})$	Plasma wavelength, λ_P (nm)	Carrier concentration, $(\times10^{20}cm^{-3})$
100	S_D	1.3043	1445.16	4.2637
200	S_E	1.6905	1115.05	7.1619
350	S_F	1.7870	1054.84	8.0029
600	S_G	1.8166	1037.63	8.2705

Using values in tables 3 and 4 we drew the graphs of carrier concentration, n_e as a function of plasma frequency, ω_P. The graphs are as shown in figures 5. It was clearly noted from the figures that the carrier concentration of all the samples increases linearly with increasing plasma frequency, ω_P. This further makes it clear that it is the carrier concentration that shifts the plasma edges towards the visible range as was shown in figures 1.
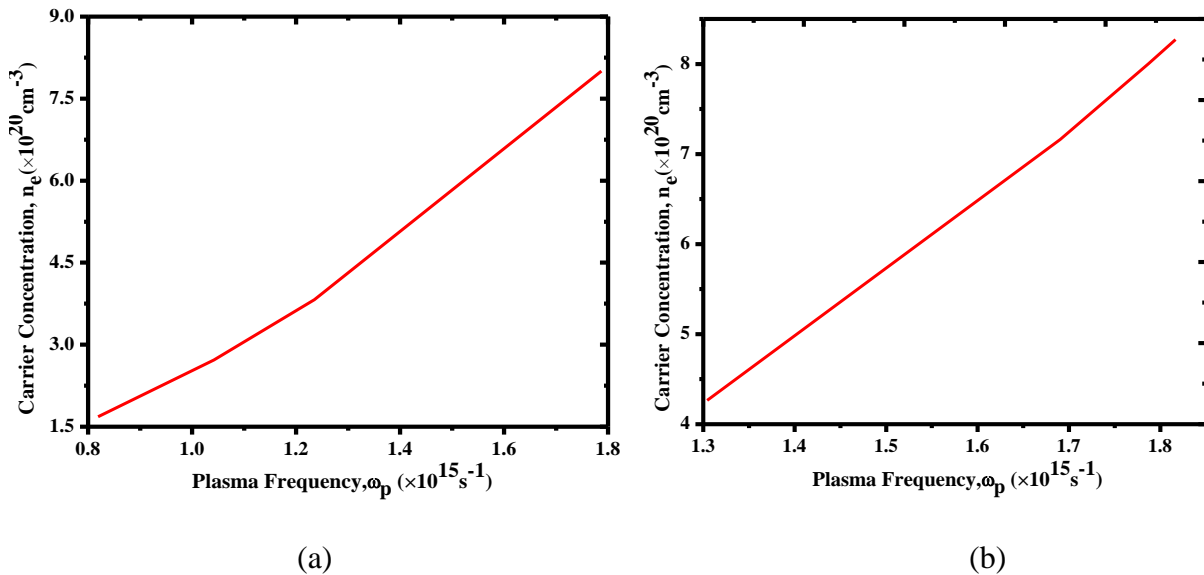

(a)　　　　　　　　　　　　　　　　　(b)

Figure 5. Carrier concentration against wavelength showing (a) various plasma frequencies of the samples and (b) various film thicknesses of the samples.

The optical band gap E_g was evaluated from the standard expression[36].

$$\alpha h v \propto (h v - E_g)^n \qquad\qquad [25]$$

where h is Planck's constant, v is the frequency and hence hv is the photon energy in electron volts (eV) and $\alpha = \dfrac{2\pi k}{\lambda}$ is the absorption coefficient. The constant n depends on the optical transition mode having the values as listed in Table 4.

The Plots of $(\alpha h v)^{\frac{1}{2}}$ versus photon energy, hv, in the high absorption region, and extrapolation of the curve to hv axis gives the indirect band gap. Similarly, $(\alpha h v)^{2}$ versus hv and extrapolating to the hv axis gives direct band gap. Tin oxide is a direct band gap material [37].

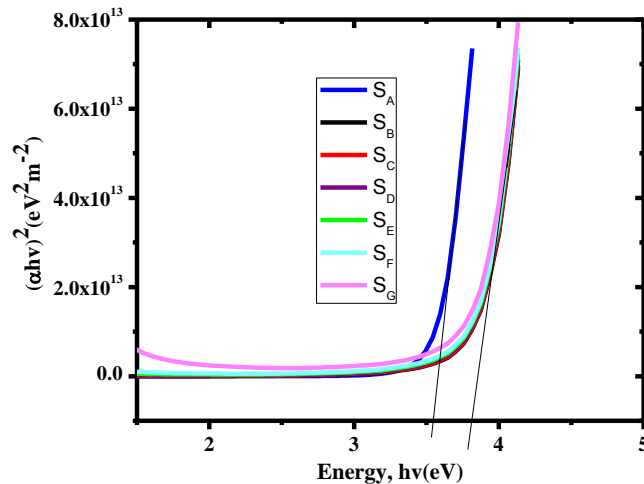**Figure 6.** $(\alpha h v)^{2}$ **Verses hv plots for determining the optical direct band gap of SnO₂ and SnO₂: F.**

Figure 6 shows plots of $(\alpha h v)^{2}$ versus photon energy, hv in high absorption region. Extrapolation of the curves to hv = 0 gave the direct band of SnO_2 and SnO_2: Ffilms in the range $3.55eV - 3.81eV$ for the undoped and heavily doped films. We found out that the direct band gap for SnO_2 to be 3.55 eV which compares well with 3.6eV as already reported[38].

Further, it was noted that there is a widening of band gap with increase of fluorine doping concentration. This widening of the band gap can be understood on the basis of Burstein–Moss shift, which occurs due to filling up of low-lying energy levels by the conduction electrons[39]. According to this well-known Burstein-Moss (BM) shift, above the Mott critical density the partial filling of the conduction band causes a blocking of the lowest states and thus a widening of the optically observed bandgap. Further, above the Mott critical density, the valence and conduction bands are shifted in energy as a result of electron-electron and electron-impurity scattering[22]. In SnO_2 these incline to partially compensate the BM shift.

Now, assuming the function of electron-electron and electron-impurity scattering, the energy gap for direct transitions in the doped material is given in terms of the unperturbed bands as shown in equation 26[22].

$$E_g^o = E_c^o\left(k_F\right) - E_v^o(k_F)$$ [26]

Alternatively, equation (26) may be expressed as shown in equation (27)

$$E_g^o = E_{g0} + \Delta E_g^{BM}$$ [27]

where the BM shift is given by equation (28)

$$\Delta E_g^{BM} = \frac{\hbar^2}{2m_{vc}^*}\left(3\pi^2 n_e\right)^{2/3}$$ [28]

with the reduced effective mass according to equation (29)

$$\frac{1}{m_{vc}^*} = \frac{1}{m_v^*} + \frac{1}{m_c^*}$$ [29]

Equation (29) predicts an energy gap shift proportional to $n_e^{2/3}$. Using equation (28) we calculated the values of BM of the samples S_D, S_E, S_F and S_G. The computed values were $2.7736 \times 10^{18}\,eV$, $3.8238 \times 10^{18}\,eV$, $4.7968 \times 10^{18}\,eV$ and $7.8470 \times 10^{18}\,eV$ respectively. From the values it was clear that the optical bandgap should increase.

Table 4: Values of the exponent nfor Equation 25 for different band gap transition modes.

Transition mode	
½	Direct allowed
3/2	Direct forbidden
2	Indirect allowed
3	Indirect forbidden

Figure 7 shows absorption spectra over the wavelength range 300 – 2500nm for the samples in figure 1(c). The absorption for each sample was calculated from the relation in equation (30). It was noted that almost all the samples have an absorption peak which shifts towards the visible range with increase in fluorine doping concentration. The shift of the position of the absorption edge can be associated to the varying bandgap.

$$T + R + A = 1$$ [30]

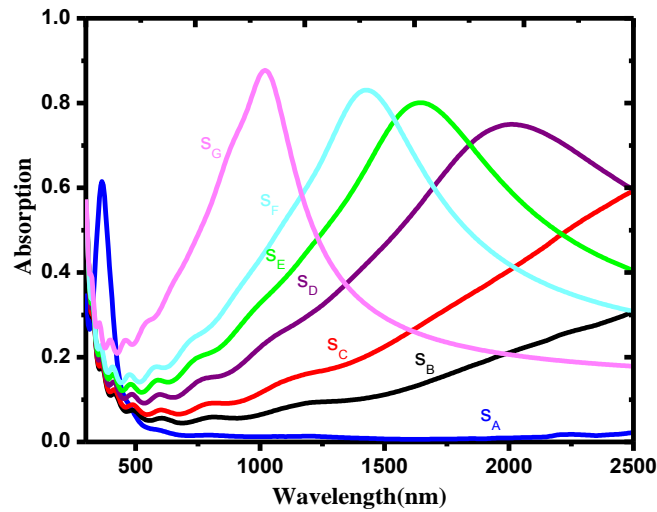where T is the transmittance, R is the reflectance and A is the absorption.

Figure 7. Spectral absorptance A = 1-(R+T) for the samples in figure 1.0 (c).

3.2 Electrical Studies.

The relationship between optical conductivity and the optical constants is as given in equation (31)[34].

$$\frac{\sigma_1}{c} = \frac{nk}{\lambda_0} \tag{31}$$

where $\lambda_0 = \dfrac{2\pi c}{\omega_0} = 12{,}850\text{nm}$.

Using the relation in equation (31) we computed the optical conductivity, σ_1 for all the samples and presented the results as shown in figure 8. It was observed from the figure that the optical conductivity increases exponentially with increasing dopant concentration. This effect illustrates that doping improves the conductivity properties of the material to a significant degree.

From figures 4(b) and 8 it is clearly observed that there is a close relationship between the optical conductivity, σ_1 and the imaginary part of the dielectric constant, ε_2.
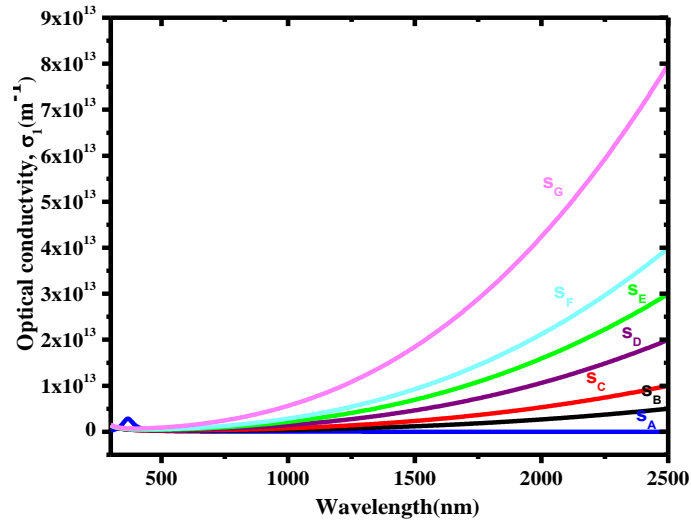
Figure 8 Optical conductivity spectra

4. Conclusion

In this work, fluorine doped tin oxide films were modeled successfully using a dielectric constant of a combined Drude and Lorentz model. From the analysis it was shown that the films had very high visual transmittance and high infrared reflectance. The results implied the possibleness of the films to be employed as spectrally selective coating materials. From the analysis it can be concluded that an increase in the doping concentration improves the optical and electrical properties of tin oxide to a greater extent. From the study it can also be concluded that the film thickness also affects the transmittance and reflectance properties of the films. An increase in film thickness leads to an increase in reflectance and a decrease in transmittance.

References

[1] C. Granqvist and A. Hultåker, "Transparent and Conducting ITO Films: New Development and Applications," pp. 1-5, 2002.

[2] Hecht, D. Hu and G. Irvin, "Emerging Transparent Electrodes Based on Thin Films of Carbon Nanotubes, Graphene and Metallic Nanostructures," *Advanced materials,* pp. 1482-1513, 2011.

[3] B.-Y. &. Jeong, M.-C. &. Moon, T.-H. &. Lee, W. &. Myoung, J.-M. &. Hwang, Jeoung-Yeon, Seo and Dae-Shik., "Transparent conductive Al-doped ZnO films for liquid crystal

displays.," *Journal of Applied Physics,* no. 99, pp. 124505-124505., 2006.

[4]   Weis and Martin., "Transparent Electrodes for Flexible Organic Light-Emitting Diodes and Displays.," *Display and Imaging.,* pp. 46-68, 2015.

[5]   P. K. Biswas, "Study of solar radiation at various incident angles on soft chemistry based transparent conducting oxide (TCO) coated window glass," *Journal of Fundamentals of Renewable Energy and Applications,* pp. 57-65, 2018.

[6]   L. E. Runnerstrom, A. Llorde, D. S. Lounisac and J. D. Milliron, "Nanostructured electrochromic smart windows: traditional materials and NIR-selective plasmonic nanocrystals," *Royal society of chemistry,* pp. 10555-10572, 2014.

[7]   S. Boscarino, I. Crupi, S. Mirabella, F. Simone and A. Terassi, "TCO/Ag/TCO transparent electrodes for solar cells application," *Applied Science A,* p. 1287–1291, 2014.

[8]   K. Angelov, H. Komitov and A. Mustafov, "Transparent conductive oxides and their shielding efficiency against electromagnetic interferences," pp. 111-115, 2015.

[9]   B. Karmakar, Functional Glasses and Glass-Ceramics, United Kingdom: Butterworth-Heinemann, 2017.

[10] 24 July 2019. [Online]. Available: https://en.wikipedia.org/wiki/Electrochemical_cell.

[11] Y.-S. Shim, H. G. Moon, D. H. Kim, H. W. Jang, C.-Y. Kang, Y. S. Yoon and Soek-JinYoona, "Transparent conducting oxide electrodes for novel metal oxide gas sensors," *Elsevier, Sensors and Actuators B,* pp. 357-363, 2011.

[12] R. Mishra, K. Sheo and S. Prakash, "Optical and gas sensing characteristics of tin oxide nano-crystalline film," *Journal of Ovonic Research,* pp. 77-85, 2009.

[13] Shamala, Murthy and Narasimha, "Studies on Tin oxide Films Prepared by Electron Beam Evaporation and Spray Pyrolysis Methods," *Indian Academy of Sciences, Bull. Material Sci.,* pp. 295-301, 2004.

[14] Chitra, Takwale, Bhide, Shailaja and Kulkarni, "Effect of Sn incorporation on the growth mechanism of sprayed SnO2 films.," *Amerrican Instute of Physics,* pp. 73-82, 1991.

[15] Z. Shanting, "Study of fluorine-doped tin oxide (FTO) thin films for photovoltaics applications," *Materials Universite Grenoble,* p. 40, 2017.

[16] Z. Wang, C. Chen, K. Wu, H. Chong and H. Ye, "Transparent conductive oxides and their applications in near infrared Plasmonics," 2019.

[17] G. Roy, "Criteria for choosing Transparent conductors," *MRS Bulletin,* pp. 52-57, 2000.

[18] G. Dobrikov, M. Rassovska, N. Andreev, S. Boyadzhiev, K. Gesheva, T. Ivanova, P. Sharlandjiev and D. Nazarowa, "Development of transparent heat mirrors based on metal

oxide thin film structures," *Thin Solid Films,* pp. 1091-1094, 2009.

[19] R. W. Ronard, "Thin-film Coatings: Understanding key design principles of antireflection coatings," *Laser Focus World,* 2016.

[20] A. Thelen, "Energy Related Optical coatings," *Optical coating laboratory,* pp. 65-80, 1981.

[21] K. Nakataa and A. Fujishima, "TiO2 photocatalysis:Design and applications," *Journal of Photochemistry and photobiology C,* pp. 169-189, 2012.

[22] H. Ivar, "Indium-Tin-Oxide Thin Films:Basic Optical Properties and applications to Energy Efficient Windows," Chalmers University of Technology, Goteborg, Sweden, 1984.

[23] C. Maghanga, *Preparation and Characterisation of a Spectrally Selective Reflector Surface Based on TiO2:Nb Thin Films.,* Eldoret: Moi University, 2009.

[24] J. (. Wanga and D. Shi, "Spectral selective and photothermal nano structured thin films for energy efficient windows," *Applied Energy 208,* pp. 83-96, 2017.

[25] F. Mark, Optical Properties of Solids, New York: Oxford University Press, 2001.

[26] C. G. Ribbing, Introduction to Material Optics, a Compendium, Sweden: Uppsala University, 2002.

[27] S. JI and R. NAB, "Effect of Processing on the Electrical Properties of Spray-Deposited SnO2:F Thin Films.," *Journal of Applied Science,* pp. 672-677, 2008.

[28] R. Swinepoxes, "Determination of Thickness and Optical Constants of Armorphous Silicon," *Journal of Physics,* p. 1214, 1983.

[29] W. Theiss and W. Teiss(Ed.), "Scout Thin film Analysis Software Handbook, Hard and Software," *Aachen, Germany,* pp. 54-57, 2001.

[30] J. S. Maudes and T. Rodrigues, "Sprayed SnO2 films: Growth Mechanism and film Structure Characterization," *Thin film solids,* pp. 183-189, 1980.

[31] M. J. Mageto, C. Maghanga, M. Mwaburi and H. Jafri, "Transparent and conducting TiO2:Nb thin films prepared by spray pyrolysis technique," *American Research Journal of Physics,* p. 63, 2015.

[32] D. Mergel and Z. Qiao, "Dielectric modelling of the optical spectra of thin In2O3:Sn films," *Journal of Physcics D: Applied Physics,* pp. 794-801, 2002.

[33] M. J. Mageto, C. Maghanga and M. Mwamburi, "The Lorentz Osillator Model simulation Illustrating a Broad Maximum in the Bulk Reflectance for Frequencies Just Above the Resonance Frequency," *The African Review of Physics,* pp. 95-105, 2012.

[34] F. Wooten, Optical Properties of Solids, New York: Academic Press, 1972.

Available online http://ir.kabarak.ac.ke/handle/123456789/1

[35] W. Q. Hong, "Extraction of extinction coefficient of weak absorbing thin films from special absorption," *Journal of Applied Physics D: Applied Physics,* vol. 22, pp. 1384-1385, 1989.

[36] C. Granqvist, Handbook of Inorganic Electrochromic Materials, the Netherlands: Elsevier, Amsterdam, 1995, pp. 265-275.

[37] E. Shanthi, V. Dutta, A. Banerjee and K. Chopra, "Electrical and Optical Properties of undoped and antimony-doped tin oxide films," *Journal of Applied Science,* pp. 6243-6253, 1980.

[38] S. Zhang, "Study of fluorine-doped tin oxide (FTO) thin fims for photovoltaics applications," *Materials Universite Grenoble Alpes,* 2017.

[39] I. Hamberg and C. Granqvist, *Appl. Phys.*

[40] Granqvist, private communication:E-beam evaporated ITO is produced commercially by OCLI, california, 1984.